The onset of thermal convection in rotating spherical shells

By E. DORMY[1], A. M. SOWARD[2], C. A. JONES[2], D. JAULT[3] AND P. CARDIN[3]

[1]Institut de Physique du Globe de Paris/CNRS, 4 place Jussieu, 75252 Paris Cedex 05, France
[2]Department of Mathematical Sciences, University of Exeter, Exeter, EX4 4QE, UK
[3]LGIT/CNRS, Université Joseph Fourier BP53, 38041 Grenoble Cedex 9, France

The correct asymptotic theory for the linear onset of instability of a Boussinesq fluid rotating rapidly in a self-gravitating sphere containing a uniform distribution of heat sources was given recently by Jones *et al.* (2000). Their analysis confirmed the established picture that instability at small Ekman number E is characterized by quasi-geostrophic thermal Rossby waves, which vary slowly in the axial direction on the scale of the sphere radius r_o and have short azimuthal length scale $O(E^{1/3}r_o)$. They also confirmed the localization of the convection about some cylinder radius $s = s_M$ roughly $r_o/2$. Their novel contribution concerned the implementation of global stability conditions to determine, for the first time, the correct Rayleigh number, frequency and azimuthal wavenumber. Their analysis also predicted the value of the finite tilt angle of the radially elongated convective rolls to the meridional planes. In this paper, we study small-Ekman-number convection in a spherical shell. When the inner sphere radius r_i is small (certainly less than s_M), the Jones *et al.* (2000) asymptotic theory continues to apply, as we illustrate with the thick shell $r_i = 0.35 r_o$. For a large inner core, convection is localized adjacent to, but outside, its tangent cylinder, as proposed by Busse & Cuong (1977). We develop the asymptotic theory for the radial structure in that convective layer on its relatively long length scale $O(E^{2/9}r_o)$. The leading-order asymptotic results and first-order corrections for the case of stress-free boundaries are obtained for a relatively thin shell $r_i = 0.65 r_o$ and compared with numerical results for the solution of the complete PDEs that govern the full problem at Ekman numbers as small as 10^{-7}. We undertook the corresponding asymptotic analysis and numerical simulation for the case in which there are no internal heat sources, but instead a temperature difference is maintained between the inner and outer boundaries. Since the temperature gradient increases sharply with decreasing radius, the onset of instability always occurs on the tangent cylinder irrespective of the size of the inner core radius. We investigate the case $r_i = 0.35 r_o$. In every case mentioned, we also apply rigid boundary conditions and determine the $O(E^{1/6})$ corrections due to Ekman suction at the outer boundary. All analytic predictions for both stress-free and rigid (no-slip) boundaries compare favourably with our full numerics (always with Prandtl number unity), despite the fact that very small Ekman numbers are needed to reach a true asymptotic regime.

1. Introduction

The classical problem of thermal convection of a Boussinesq fluid in rotating self-gravitating spheres and shells has a long history and continues to be of interest because of its geophysical and astrophysical applications, but also because it concerns fundamental issues in rotating fluid dynamics. The nature of the onset of convection in spheres in the rapidly rotating limit of small Ekman number E leads to a difficult asymptotic problem discussed by Roberts (1965). Asymptotic solutions were proposed by Roberts (1968) and Busse (1970), but the correct asymptotic solution for full spheres was given by Jones, Soward & Mussa (2000 hereinafter referred to as JSM).

We summarize briefly the nature of the onset of convection in a full sphere owing to a uniform distribution of heat sources. It has long been known, and stressed in Busse's pioneering papers (Busse 1970, 1975) and reviews (Busse 1994, 2002), that motion at small Ekman number is quasi-geostrophic almost independent of the coordinate z parallel to the rotation axis. Now in spheres (and shells), true geostrophic motion is azimuthal; it does not convect heat and so does not constitute the mode of convective instability. Onset of instability is characterized instead by quasi-geostrophic thermal Rossby waves, which vary slowly in the z-direction on the length scale r_o, namely the sphere radius. To overcome the two-dimensional constraints of the Taylor–Proudman theorem, viscous forces must be invoked on short length scales of order $E^{1/3}r_o$ in the cylindrical radial s- and azimuthal ϕ-directions. Indeed, Roberts (1968) proposed separable solutions with azimuthal wavenumber $M = O(E^{-1/3})$, which are localized in the radial direction about some cylinder $s = s_L$. Busse (1970), besides correcting the symmetry of the solution with respect to the equatorial plane, explained this phenomenon by noting that, on the one hand, the slope of the outer spherical boundary is the reason for forcing convective flow to be three-dimensional; so this inhibition is smallest for small s near the rotation axis. On the other, he argued that the quasi-geostrophic motion is largely driven by the radial s-component of gravity, which increases with s and is maximized at the equator $s = r_o$ of the outer sphere. Evidently, the aforementioned processes compete with one another leading to convection which is located on the cylinder with s_L roughly $r_o/2$ but quantitatively dependent on the value of the Prandtl number P. Since viscous dissipation on the short $O(E^{1/3}r_o)$ length scale is so great, the critical Rayleigh number necessary to cause the fluid to convect is large, of order $E^{-4/3}$.

Soward (1977) noted that the Roberts–Busse asymptotic theory had associated with it a fundamental difficulty, which is best resolved by anticipating a WKB-asymptotic expansion of the convective mode in terms of a complex radial wavenumber $K(s)$, determined as a function of s by the solution of some dispersion relation $\Omega(s, K) = \text{constant}$, the frequency of the convection. According to the Roberts–Busse theory, localized convection is associated with the location $s = s_L$ at which $K(s_L) = 0$. In the vicinity of this point, the group velocity $\partial\Omega/\partial K$ vanishes and the WKB-approximation breaks down and a second-order amplitude equation of the form (3.18) below must be considered instead. This is of complex Airy equation type with a single turning point. It has no localized solution, i.e. it has no solution that does not diverge on at least one side of the cylinder. Herein lies the success of the JSM approach, which follows the procedures outlined by Yano (1992) for a simplified problem based on a variant of Busse's (1970) annulus model. Instead of constructing an amplitude equation of Airy function type, an equation with two turning points is required. Criticality occurs when the turning points are almost coincident at some location $s = s_c$, where phase mixing $\partial\Omega/\partial s$ vanishes. This turns out to be a complex

location and it is conditions there that resolve the eigenvalue problem. The most striking feature of the solution found by JSM meeting these so-called global stability criteria, $(\partial\Omega/\partial s)_c = 0$ and $(\partial\Omega/\partial K)_c = 0$ (Huerre & Monkewitz 1990), is that the critical Rayleigh number for the onset of convection found this way exceeds that determined by the Roberts–Busse local theory, but agrees correctly with numerical simulations. It is important to note that convection is still localized close to some cylinder $s = s_M$, which is, however, different to the value $s = s_L$ predicted by local theory. For the Prandtl number unity case

$$P = 1\,, \tag{1.1}$$

which we will consider, these key radii are

$$s_L/r_o \approx 0.5004, \qquad s_c/r_o \approx 0.5342 - 0.09667\,\mathrm{i}, \qquad s_M/r_o \approx 0.5915, \tag{1.2a–c}$$

where the value of s_L was first obtained by Busse (1970), while the values of s_c (complex, as anticipated above) and s_M were determined by JSM.

In this paper, we investigate small-Ekman-number convection for a fluid shell corresponding to the geophysical situation when there is a solid inner core, radius r_i. Within the framework of local theory, Busse & Cuong (1977) point out that the critical Rayleigh number for localized columnar convection inside the inner sphere tangent cylinder $s = r_i$ decreases with increasing s and reduces its magnitude discontinuously by yet a further factor of about $\frac{1}{4}$ as the tangent cylinder is crossed into the exterior region $s > r_i$. Accordingly, the minimum local Rayleigh number for the complete shell occurs either at the local sphere minimum $s = s_L$ outside the tangent cylinder, when the inner core radius is smaller, i.e. $r_i < s_L$, or adjacent to the tangent cylinder $s = r_i$ when $r_i > s_L$. Our contention is that local theory is valid in the latter thin-shell case, when the radius aspect ratio $\eta = r_i/r_o$ satisfies

$$\eta > s_L/r_o\,. \tag{1.3}$$

Then convection is localized in a thin layer outside, but next to, the tangent cylinder, where conditions for convection are most favourable. Therefore one of our main objectives is to determine the radial structure of these tangent cylinder modes for $E \ll 1$ by a higher-order asymptotic theory; in so doing, we also determine the departures of the Rayleigh number and frequency from their local theory values. We then compare those predictions with the full numerical solutions of the governing partial differential equations at small Ekman number.

In contrast, for sufficiently small inner core, the JSM global theory applies, predicting convection localized in the vicinity of the cylinder $s = s_M$ (see (1.2c)) with $r_i < s_M < r_o$. The asymptotic theory for these interior modes, however, is only valid when the intersections s_- and s_+ with the real axis of the anti-Stokes lines emanating from the critical complex location s_c lie within the fluid region, i.e. $r_i \leqslant s_- \leqslant s_+ \leqslant r_o$. For our Prandtl number unity case (1.1), JSM determined those values to be

$$s_-/r_o \approx 0.4634, \qquad s_+/r_o \approx 0.7536. \tag{1.4a, b}$$

Since the JSM global interior mode theory is only applicable in the thick shell case

$$\eta < s_-/r_o, \tag{1.5}$$

there is an range of aspect ratios $s_-/r_o < \eta < s_L/r_o$, namely $0.4634 < \eta < 0.5004$ when $P = 1$, for which neither of the proposed asymptotic theories applies. What happens in this intermediate range is a very delicate matter which lies outside the

scope of our analysis. For that reason, we focus on the thick-shell $\eta = 0.35$ and thin-shell $\eta = 0.65$ cases, which lie comfortably in the parameter ranges (1.5) and (1.3), respectively, where each type of mode is clearly distinguishable.

Gilman's (1975) early numerical solutions of the shell problem focused on Prandtl number unity. Later studies, beginning with Zhang & Busse (1987), considered the effect of varying P. Since a complete parameter search is a formidable undertaking, which would in fact obscure our main points, we will follow Gilman (1975) and restrict attention to the case $P = 1$ throughout this paper. Following on from those early studies, there have been many numerical calculations concerning the onset of instability in spherical shells (see e.g. Zhang 1991, 1992; Zhang & Jones 1993; Ardes, Busse & Wicht 1997; also the review by Busse 2002).

As an aside we remark that, on decreasing the Prandtl number, convection tends to be less localized and spreads radially towards the equator $s = r_o$ of the outer sphere. It means that far smaller Ekman numbers than considered here are needed to attain true asymptotic regimes. That is not the only issue; for, on decreasing P to very small values, new modes located near the equator of the outer sphere may be preferred (Zhang & Busse 1987; Zhang 1995; Zhang & Roberts 1997), which are outside the scope of our theory.

In addition to the usually adopted internal heating case, we wish to address the more general situation for which the temperature $T(r)$ on the inner and outer spheres is prescribed: $T_i \equiv T(r_i)$ and $T_o \equiv T(r_o)$. When the heat sources are distributed uniformly, the temperature profile generally contains terms proportional to both r^2 and r^{-1} (see e.g. Chandrasekhar 1961). We, however, will restrict attention to only two particular cases, namely

$$
T(r) = \begin{cases} -\dfrac{T_i - T_o}{r_o^2 - r_i^2}\, r^2 + \dfrac{r_o^2 T_i - r_i^2 T_o}{r_o^2 - r_i^2} & \text{for internal heating,} \quad (1.6a) \\[2mm] \dfrac{r_i r_o (T_i - T_o)}{r_o - r_i}\, r^{-1} + \dfrac{r_o T_o - r_i T_i}{r_o - r_i} & \text{for differential heating.} \quad (1.6b) \end{cases}
$$

The former 'internal heating' case is motivated by the situation for a complete sphere ($r_i = 0$) for which the uniform heat source distribution leads to the temperature gradient $-\beta r$, where $\beta \equiv 2(T_i - T_o)/r_o^2$ (see also Chamberlain & Carrigan 1986). In the latter 'differential heating' case, there are no internal heat sources and the temperature gradient is simply maintained by the temperature difference between the inner and outer boundaries (see, e.g. Carrigan & Busse 1983).

The case of differential heating has an interesting feature, namely since the magnitude of the temperature gradient ($\propto r^{-2}$) increases so rapidly with decreasing r, the onset of instability is always associated with a tangent cylinder mode whatever the inner core radius. Thus, as an illustrative example, we continue to take the aspect ratio $\eta = 0.35$ motivated by the Earth's fluid core, for which there is continuing interest (see, e.g. Busse 2002; Ishihara & Kida 2002) in geodynamo applications.

As well as our investigations of the cases with stress-free boundaries, we also consider the solutions in the case of rigid boundaries at which we apply a no-slip boundary condition. This is, of course, the true situation in the Earth's context as well as for experiments (Busse & Carrigan 1976; Carrigan & Busse 1983; Chamberlain & Carrigan 1986; Hart, Glatzmaier & Toomre 1986; Cordero & Busse 1992). In that case, an Ekman layer forms at the boundary outside which the mainstream solution on the short $E^{1/3}$ azimuthal length scale is influenced at $O(E^{1/6})$ by Ekman-layer suction, as noted by Zhang & Jones (1993). We incorporate the

Ekman-layer corrections into the stress-free asymptotics and compare the results with the full numerics. (Incidentally, boundary-layer corrections, though not of the Ekman-layer type, have been implemented in similar asymptotic problems by Jones, Mussa & Worland (2003) in the context of rotating magnetoconvection.) Full numerical investigations employing both stress-free and no-slip boundary conditions for aspect ratios $\eta = 0.4$ and 0.8 were undertaken by Zhang & Jones (1993). Whereas the smaller value is motivated by the Earth's core, the latter value is appropriate to the Jovian atmosphere. Since the gap width ratio $(r_o - r_i)/r_o$ is so small, namely 0.2 for $\eta = 0.8$, the equatorial boundary of the outer sphere strongly influences the solution and it is difficult to attain a true asymptotic regime. That is why we adopted the larger gap width ratio 0.35 corresponding to $\eta = 0.65$.

We outline the organization of our paper. In §2, we briefly summarize the governing equations and describe the numerical methods used to solve them. In §3, we develop the local theory necessary to obtain our asymptotic results. The WKB-method, used to determine the radial structure, is explained in §3.1; it leads to a local dispersion relation, which provides the key to the lowest-order solutions. Since the theory for interior modes is developed elsewhere by JSM, we focus attention in §3.2 instead on the higher-order resolution of the tangent cylinder modes, which are confined to a convection layer $0 \leqslant s - r_i = O(E^{2/9})$; thick compared to the short azimuthal length scale $O(E^{1/3})$. The Ekman boundary layer corrections for rigid (no-slip) boundaries to the stress-free boundary solutions are explained in §3.3. Results for internal heating are discussed in §4, where the cases of small and large inner cores are developed in §§4.1 and 4.2, respectively. The results of §5 for differential heating, which possesses a relatively steep temperature gradient, highlight the difficulty of reaching a true asymptotic limit with an expansion parameter as small as $E^{1/9}$. We comment on the role of the thinner ageostrophic boundary layer only of width $O(E^{1/3})$ on the tangent cylinder in §6.

2. The governing equations and their numerical solution

We consider a shell of inner and outer radii r_i and r_o, respectively, which rotates at constant angular velocity $\boldsymbol{\Omega}$. It is filled with Boussinesq fluid with coefficient of thermal expansion α, thermal conductivity κ and kinematic viscosity ν. The gravity field is assumed to be $-g\boldsymbol{r}$.

The linearized equations governing perturbations to the basic state are non-dimensionalized using the outer sphere radius r_o for the unit of length, the viscous time scale r_o^2/ν for the unit of time, while for our unit of temperature we adopt $-\nu r_o T_o'/\kappa$, where

$$T_o' \equiv \frac{\mathrm{d}T}{\mathrm{d}r}(r_o)\,(<0) \tag{2.1}$$

is the temperature gradient on the outer boundary. Upon introducing the dimensionless parameters

$$E = \frac{\nu}{2\Omega r_o^2}, \qquad R = -\frac{g\alpha T_o' r_o^5}{\nu\kappa}, \qquad P = \frac{\nu}{\kappa}, \qquad \eta = \frac{r_i}{r_o}, \tag{2.2a--d}$$

namely, the Ekman, Rayleigh, Prandtl numbers and aspect ratio, respectively, our linearized equations of motion and continuity for the velocity $\boldsymbol{u}$ become

$$\frac{\partial \boldsymbol{u}}{\partial t} + E^{-1}\widehat{\boldsymbol{z}} \times \boldsymbol{u} = -\nabla p + R\theta\boldsymbol{r} + \nabla^2\boldsymbol{u}, \qquad \nabla \cdot \boldsymbol{u} = 0 \tag{2.3a, b}$$

from which the vorticity equation

$$\frac{\partial}{\partial t}\nabla \times \boldsymbol{u} - E^{-1}\frac{\partial \boldsymbol{u}}{\partial z} = -R\boldsymbol{r} \times \nabla\theta + \nabla^2\nabla \times \boldsymbol{u} \qquad (2.3c)$$

follows, while the heat conduction equation for the temperature θ reduces to

$$P\frac{\partial \theta}{\partial t} = \mathscr{Q}\boldsymbol{u}\cdot\boldsymbol{r} + \nabla^2\theta, \qquad (2.3d)$$

where

$$\mathscr{Q}(r) = \begin{cases} 1 & \text{for internal heating,} & (2.3e) \\ 1/r^3 & \text{for differential heating.} & (2.3f) \end{cases}$$

The formulation for the internal heating case is identical to that of JSM. The differential heating case is similar except for the nature of the buoyancy source $\mathscr{Q}(r)$ in (2.3d). Though both cases are solved subject to isothermal boundary conditions $\theta = 0$ on the inner ($r = \eta$) and outer ($r = 1$) boundaries, we solve separately the cases of no-slip ($\boldsymbol{u} = \boldsymbol{0}$) and stress-free ($\boldsymbol{r}\cdot\boldsymbol{u} = 0$, $\boldsymbol{r}\cdot\nabla[\boldsymbol{r} \times \boldsymbol{u}/r^2] = 0$) boundary conditions.

Like JSM, we use a radial toroidal–poloidal decomposition for the numerical solution

$$\boldsymbol{u} = \nabla \times \mathscr{T}\boldsymbol{r} + \nabla \times \nabla \times \mathscr{S}\boldsymbol{r} \qquad (2.4)$$

of the velocity field and seek separable solutions proportional to

$$\mathscr{E}(\phi, t) \equiv \exp[\mathrm{i}(M\phi - \Omega t)]. \qquad (2.5)$$

The algorithm, which we use for the numerical solution of the ensuing eigenvalue problem for complex Ω at fixed M and R, differs slightly from that employed by JSM. Specifically, we adopt a grid discretization in radius (instead of a spectral decomposition) and the equations are time stepped until an exponentially growing mode is identified.

Within the toroidal–poloidal framework (2.4), the governing equations are discretized using finite differences on a radial grid which contains between 140 and 1200 points. The grid is stretched near the boundaries following a geometric progression, so as to avoid introducing localized error terms associated with the truncation. The number chosen to obtain accurate resolution of the boundary layers is model dependent and guided by a convergence study of Dormy, Cardin & Jault (1998) of a situation in which the primary flow is driven by Ekman suction. The scalar fields $\mathscr{T}$, $\mathscr{S}$ and θ are then expanded in terms of between 80 and 800 spherical harmonics. The diffusion terms are managed with Crank–Nicholson time stepping, all other terms (including the Coriolis terms) are integrated with a second-order Adams–Bashforth scheme. Further description of our numerical algorithm can be found in Dormy (1997), Dormy *et al.* (1998) and Christensen *et al.* (2001), albeit for different applications. Since then, major improvements to our computer code have resulted from the parallelization of the algorithm on distributed memory computers, which take advantage of the radial finite-difference scheme through a domain decomposition in the radial direction using a modified LU decomposition for the pentadiagonal operator (see Lakshmivarahan & Dhall 1990). We emphasize that our numerical algorithm does not solve an eigenvalue problem, but integrates the equations in time instead. To estimate the eigenvalue numerically, we time step the linearized system until a steady exponential growth rate can be identified accurately. By varying the Rayleigh number, the growth rate can be adjusted until it is extremely close to

zero (positive or negative). Once achieved, the critical Rayleigh number is readily estimated through linear interpolation. This process is repeated until the Rayleigh number converges. The frequency of the eigenmode can then be estimated accurately with finite differences (see Dormy 1997). We found that this approach is efficient throughout the parameter range investigated; indeed, accurate results were obtained by this method even at very small Ekman numbers.

3. The asymptotic analysis

In this section, we develop the asymptotic theory used to determine the radial structure and to solve the eigenvalue problem. The solution depends in part on the WKB-representation which we outline in §3.1. Two types of convective mode are possible. One type is the interior modes which are localized in the neighbourhood of a cylinder $s = s_M$ away from the tangent cylinder $s = \eta$ of the inner sphere, such that $\eta < s_M < 1$. The other type is a wall mode which is localized adjacent (but exterior) to the tangent cylinder with $s_M = \eta$. The key, however, to the solution in both cases is the correct treatment of an amplitude equation valid near a certain critical radius s_c. JSM developed the appropriate asymptotic theory for the interior modes for which s_c takes a complex value in the vicinity of the real value s_M. Here, we describe the corresponding theory for the tangent cylinder modes in §3.2 with $s_c = s_M = \eta$, for which the appropriate amplitude equation (3.18) differs from that considered by JSM. Such modes with a similar amplitude equation have been encountered in other contexts (see e.g. Meunier *et al.* 1997) and their nature is described in Soward's (2003) review.

3.1. *The local dispersion relation*

In the small-Ekman-number limit

$$E \ll 1, \tag{3.1}$$

it is convenient to adopt cylindrical polar coordinates s, ϕ, z and adopt the axial toroidal–poloidal decomposition

$$\boldsymbol{u} = \nabla \times \Psi \widehat{z} + \nabla \times \nabla \times \Phi \widehat{z} \tag{3.2a}$$

for the velocity. At leading order, the vorticity equation (2.3c) implies that $\partial \boldsymbol{u}/\partial z \approx 0$. To resolve the ensuing geostrophic degeneracy, we seek short-length-scale quasi-geostrophic solutions localized radially in the vicinity of the cylinder $s = s_M$ for which Ψ and Φ vary rapidly in the azimuthal ϕ- and radial s-directions, but slowly in the axial z-direction. These assumptions allow us to make the quasi-geostrophic approximation

$$\boldsymbol{u} \approx \nabla \times \Psi \widehat{z} + W \widehat{z}, \qquad p \approx -E^{-1}\Psi \qquad (W = \widehat{z} \cdot \nabla \times \nabla \times \Phi \widehat{z}), \tag{3.2b}$$

supplemented by

$$\nabla \times \boldsymbol{u} \approx \Upsilon \widehat{z} + \nabla \times W \widehat{z} \qquad (\Upsilon = \widehat{z} \cdot \nabla \times \nabla \times \Psi \widehat{z}), \tag{3.2c}$$

in which z-derivatives are neglected. This provides us with sufficient accuracy for our asymptotic analysis and is consistent with the approximations made by previous authors (Roberts 1968; Busse 1970). Indeed, following JSM, we suppose that the radial s-structure is of WKB-type:

$$\mathscr{K}(s) \equiv \exp\left(\mathrm{i}\int K\,\mathrm{d}s\right) \qquad (|K| \gg 1). \tag{3.3}$$

Within the framework of the approximations (3.2b, c) we obtain the expressions

$$\boldsymbol{r \cdot u} \approx \mathrm{i}M\Psi + zW, \qquad \boldsymbol{r \cdot \nabla \times u} \approx z\Upsilon + \mathrm{i}MW \qquad (\Upsilon = A^2\Psi), \qquad (3.4a, b)$$

for the radial velocity and vorticity, where the local wavenumber A is given by

$$A^2 = K^2 + M^2/s^2. \qquad (3.5)$$

The idea is that the columnar convection in the vicinity of the cylinder $s = s_M$ is localized outside the tangent cylinder $s = \eta$ (i.e. $s_M \geqslant \eta$). An Ekman layer, width $O(E^{1/2})$, forms at the intersection of the cylinder $s = s_M$ with the outer boundary. The jump conditions across the Ekman layer determine the boundary condition on the mainstream velocity. In the case of stress-free boundaries, the Ekman layer is weak and can be ignored; whereas in the case of no-slip boundaries, the Ekman layer induces a small radial flow. Correct to lowest order, we have the reduced boundary conditions

$$\boldsymbol{r \cdot u} \approx \begin{cases} 0 & \text{stress-free,} & (3.6a) \\[2mm] -\sqrt{\dfrac{Er}{2z}}\,\boldsymbol{r \cdot \nabla \times u} & \text{no-slip,} & (3.6b) \end{cases}$$

at $r = 1$ on the mainstream flow for the cases of slippery and rigid outer boundaries, respectively. The Ekman suction boundary condition (3.6b) follows from Greenspan's (1968) equation (2.6.15) on the assumption that the velocity $\boldsymbol{u}$ varies on a short length scale, here $O(E^{1/3})$. Specifically, the corrections due to boundary-layer curvature have been neglected.

In our small-Ekman-number quasi-geostrophic limit, axial z-components of the vorticity equation (2.3c) and the equation of motion (2.3a), together with the heat conduction equation (2.3d), yield correct to lowest order, the equations

$$E(A^2 - \mathrm{i}\Omega)(A^2\Psi) - \frac{\mathrm{d}W}{\mathrm{d}z} = -\mathrm{i}MER\theta, \qquad (3.7a)$$

$$E(A^2 - \mathrm{i}\Omega)W - \frac{\mathrm{d}\Psi}{\mathrm{d}z} = zER\theta, \qquad (3.7b)$$

$$(A^2 - \mathrm{i}P\Omega)\theta = \mathscr{Q}\,(\mathrm{i}M\Psi + zW), \qquad (3.7c)$$

respectively, where the only z-derivatives retained stem directly from the large Coriolis acceleration. We solve these coupled equations subject to the boundary conditions (3.6) on $z = h(s)$, where

$$h(s) = \sqrt{1 - s^2}, \qquad (3.8)$$

and the symmetry condition $W = 0$ on the equatorial plane $z = 0$.

We follow JSM and introduce the further scalings

$$\left. \begin{aligned} &R = E^{-4/3}\mathscr{R}, & &(M, K, A) = E^{-1/3}(m, k, a), & &\Omega = E^{-2/3}\omega, \\ &\theta = \theta, \quad \Psi = E^{-1/3}\psi, & &\boldsymbol{r \cdot u} = E^{-2/3}rv_r, & &\boldsymbol{r \cdot \nabla \times u} = E^{-1}r\zeta, \\ &W = E^{-2/3}w, & &(\mathrm{i}M\Psi/s, -\partial\Psi/\partial s) \approx E^{-2/3}(v_s, v_\phi), \end{aligned} \right\} \quad (3.9)$$

where we have introduced the radial and azimuthal velocities v_s, v_ϕ, whose values we plot in later figures. In this way, we can solve (3.7a, c) for θ and ψ in terms of w and

so obtain the following relations:

$$\frac{\theta}{\mathscr{Q}} = \frac{r v_r}{(a^2 - iP\omega)}, \qquad r v_r = -\frac{1}{\mathscr{F}}\left[im\frac{\mathrm{d}w}{\mathrm{d}z} + a^2(a^2 - i\omega)\, zw \right], \qquad (3.10a, b)$$

$$\psi = -\frac{1}{\mathscr{F}}\left[\frac{\mathrm{d}w}{\mathrm{d}z} - \frac{im\mathscr{R}\mathscr{Q}}{a^2 - iP\omega}\, zw \right], \qquad r\zeta = -\frac{1}{\mathscr{F}}\left[a^2 z\frac{\mathrm{d}w}{\mathrm{d}z} - im\mathscr{G}w \right], \qquad (3.10c, d)$$

where

$$\mathscr{F} = \frac{m^2\mathscr{R}\mathscr{Q}}{a^2 - iP\omega} - a^2(a^2 - i\omega), \qquad \mathscr{G} = \frac{(m^2 + a^2 z^2)\mathscr{R}\mathscr{Q}}{a^2 - iP\omega} - a^2(a^2 - i\omega), \qquad (3.10e, f)$$

in which

$$a^2 = k^2 + \frac{m^2}{s^2}, \qquad m^2 + a^2 z^2 = k^2 z^2 + \frac{m^2 r^2}{s^2}, \qquad r^2 = s^2 + z^2. \qquad (3.10g\text{–}i)$$

Substituting the expressions (3.10a–c) into (3.7b) determines the single second-order ordinary differential equation

$$\mathscr{F}\frac{\mathrm{d}}{\mathrm{d}z}\left(\frac{1}{\mathscr{F}}\frac{\mathrm{d}w}{\mathrm{d}z} \right) + \left[(a^2 - i\omega)\mathscr{G} - \frac{im}{a^2 - iP\omega}\mathscr{F}\frac{\mathrm{d}}{\mathrm{d}z}\left(\frac{\mathscr{R}\mathscr{Q}z}{\mathscr{F}} \right) \right] w = 0. \qquad (3.11)$$

It must be solved subject to the reduced boundary conditions (3.6a, b), which using (3.10b, d) become (correct to order $E^{1/6}$)

$$\frac{\mathrm{d}w}{\mathrm{d}z} - \frac{ia^2}{m}(a^2 - i\omega)zw = \begin{cases} 0 & \text{stress-free,} & (3.12a) \\[2mm] E^{1/6}\sqrt{\dfrac{r}{2z}}\dfrac{m^2 + a^2 z^2}{m^2}\mathscr{F}\, w & \text{no-slip,} & (3.12b) \end{cases}$$

at the outer boundary $z = h(s)$, equivalently $r = 1$, while our required symmetry across the equatorial plane imposes $w = 0$ on $z = 0$. In the internal heating case, the problem (3.11), (3.12a) reduces to the Roberts–Busse formulation employed by JSM, while in the differential heating case, there are links with the Carrigan & Busse (1983) formulation. That latter case is, however, essentially different because they employ a cylindrical radial gravity field, which leads to a thermal wind in the basic state before convection occurs.

An aspect of the asymptotic formulation (3.11), (3.12) is that $\mathscr{R}$ and $\mathscr{Q}$ never appear separately, but always as the product $\mathscr{R}\mathscr{Q}$. In that spirit, the quotient $\theta/\mathscr{Q}$ in (3.10a) is perhaps a better measure of the buoyancy than the temperature θ and so we will employ it in our figure 6 below, for the differential heating case $\mathscr{Q} = 1/r^3$ (see (2.3f)).

From one point of view, the solution of the eigenvalue problem (3.11), (3.12) determines the complex eigenvalue

$$\omega = \omega(s, k, m, \mathscr{R}, E), \qquad (3.13a)$$

which provides at fixed m, $\mathscr{R}$ and E, a local dispersion at given s between the complex wavenumber k and frequency ω. The stress-free problem is independent of E giving us the eigenvalue

$$\omega = \omega^{\mathrm{SF}}(s, k, m, \mathscr{R}) \qquad (3.13b)$$

with corresponding eigenfunction $w^{\mathrm{SF}}(z)$. Thus, we solve this problem and then determine the rigid boundary (no-slip) eigenvalue correction in the form

$$\omega = \omega^{\mathrm{NS}}(s, k, m, \mathscr{R}) \approx \omega^{\mathrm{SF}}(s, k, m, \mathscr{R}) + E^{1/6}\omega_1^{\mathrm{NS}}(s, k, m, \mathscr{R}) \qquad (3.13c)$$

with corresponding eigenfunction correction $E^{1/6}w_1^{NS}(z)$. Essentially, we set up the inhomogeneous problem at $O(E^{1/6})$ for $w_1^{NS}(z)$, but do not actually solve for the correction. Instead, the consistency condition, that this problem has a solution, determines ω_1^{NS}. This is a tedious but routine calculation which is helped somewhat by the fact the homogeneous stress-free problem is self-adjoint.

The alternative point of view, which we wish to emphasize, is that for the physically realized solution, the value of ω is fixed and so the dispersion relation determines the complex value of k as a function of s. In summary, therefore, our WKB-solution has the structure

$$[\theta, \psi, w]^T(s, \phi, z, t) \equiv \mathscr{A}(s)[\widehat{\theta}, \widehat{\psi}, \widehat{w}]^T(s, z)\mathscr{K}(s)\mathscr{E}(\phi, t), \qquad (3.14)$$

where $\mathscr{K}(s) \equiv \exp(i \int K \mathrm{d}s)$ (see (3.3)) varies rapidly on the short $O(E^{1/3})$ length scale, $\mathscr{E}(\phi, t) \equiv \exp[i(M\phi - \Omega t)]$ (see (2.5)). The amplitude modulation $\mathscr{A}(s)$ varies on the $O(1)$ length scale of the shell and is determined as a function of s by a higher-order theory. Of course, that modulation is dependent on the normalization of the solution $\widehat{w}(s, z)$ of the eigenvalue problem (3.11), (3.12), which itself is only determined up to a multiplicative function of s.

3.2 *The tangent cylinder modes*

The asymptotic treatment of the tangent cylinder modes is relatively straightforward. We simply start with our dispersion relation (3.13b) as determined by the lowest-order eigenvalue problem (3.11) and (3.12a), which is independent of E. We evaluate (3.13b) at $s = \eta$ and minimize $\mathscr{R}$ over all real k and m subject to the constraint $\mathrm{Im}\{\omega\} = 0$. We find that this local minimum occurs at $k = 0$ and, in this way, we determine the remaining critical values $\mathscr{R}_c$, m_c and ω_c. This minimization ensures that, when evaluated at $(s, k, m, \mathscr{R}, \omega) = (\eta, 0, m_c, \mathscr{R}_c, \omega_c)$, we have

$$\left(\frac{\partial \omega}{\partial k}\right)_c = 0, \qquad \mathrm{Im}\left\{\left(\frac{\partial \omega}{\partial m}\right)_c\right\} = 0, \qquad (3.15a, b)$$

where $m(= M/E^{1/3})$ is regarded as a continuous variable.

Since we are looking at a mode with a radial wavenumber $k = 0$ on the tangent cylinder, its WKB-structure (3.3) in the vicinity of $s = \eta$ varies on a relatively long radial length scale. Specifically, the Taylor series expansion of (3.13b) at fixed $\mathscr{R}$, ω and m determines

$$\frac{1}{2}\left(\frac{\partial^2 \omega}{\partial k^2}\right)_c k^2 + \left(\frac{\partial \omega}{\partial s}\right)_c (s - \eta) \approx 0 \qquad (3.16a)$$

which gives

$$k \approx \left[-2\left(\frac{\partial \omega}{\partial s}\right)_c \Big/ \left(\frac{\partial^2 \omega}{\partial k^2}\right)_c\right]^{1/2} (s - \eta)^{1/2}, \qquad (3.16b)$$

where the square root is taken to have positive imaginary part. Use of (3.3) determines the exponential behaviour

$$\mathscr{K}(s) \approx \exp\left\{i\left[-\frac{8}{9}\left(\frac{\partial \omega}{\partial s}\right)_c \Big/ \left(\frac{\partial^2 \omega}{\partial k^2}\right)_c\right]^{1/2} \frac{(s - \eta)^{3/2}}{E^{1/3}}\right\}, \qquad (3.16c)$$

valid for $E^{2/9} \ll s - \eta \ll 1$, which decays with increasing s. Importantly, (3.16c) identifies the relatively long radial length scale $O(E^{2/9})$ on which the WKB approximation fails. On that length scale, we replace the product $\mathscr{A}(s)\mathscr{K}(s)$ in (3.14)

by $\mathscr{W}$ and consider the alternative representation

$$w \approx \mathscr{W}(x)\,\widehat{w}_c(s,z)\,\mathscr{E}(\phi,t) \qquad \text{with} \qquad x = E^{-2/9}(s-\eta), \qquad (3.17a,b)$$

where $\widehat{w}_c(s,z)$ is simply $\widehat{w}(s,z)$, namely the solution of (3.11) subject to (3.12a) for the critical values $\mathscr{R}_c,\ \omega_c,\ m_c$ at s with the corresponding $k(s)$. Thus the amplitude function $\mathscr{W}(x)$ satisfies

$$-\frac{1}{2}\left(\frac{\partial^2\omega}{\partial k^2}\right)_c \frac{\mathrm{d}^2\mathscr{W}}{\mathrm{d}x^2} + \left(\frac{\partial\omega}{\partial s}\right)_c x\mathscr{W} + \mathscr{R}_1\left(\frac{\partial\omega}{\partial\mathscr{R}}\right)_c \mathscr{W} - \left[\omega_1 - \left(\frac{\partial\omega}{\partial m}\right)_c m_1\right]\mathscr{W} = 0,$$
$$(3.18)$$

where we have assumed the expansions

$$R = E^{-4/3}\left(\mathscr{R}_c + E^{2/9}\mathscr{R}_1 + \cdots\right), \qquad (3.19a)$$

$$\Omega = E^{-2/3}\left(\omega_c + E^{2/9}\omega_1 + \cdots\right), \qquad (3.19b)$$

$$M = E^{-1/3}\left(m_c + E^{2/9}m_1 + \cdots\right). \qquad (3.19c)$$

It is important to note that $\mathscr{E} \equiv \exp[i(M\phi - \Omega t)]$ in (3.17a) uses these actual values and not the neighbouring critical values used to determine $\widehat{w}_c(s,z)$.

The required solution $\mathscr{W}(x)$ must have the asymptotic behaviour $\mathscr{A}(s)\mathscr{K}(s)$ given by (3.16c) when $x \gg 1$ so as to match with our WKB-solution (3.14) valid for $s - \eta \gg E^{2/9}$. A thinner ageostrophic boundary-layer of width $O(E^{1/3})$ is located on the tangent cylinder connecting quasi-geostrophic behaviour on either side, where $|s - \eta| \gg E^{1/3}$. As we remarked in §1, conditions inside the tangent cylinder are unfavourable for convection. Therefore the purpose of the $E^{1/3}$-ageostrophic layer is to reduce the amplitude of the motion $\boldsymbol{u}$ and the temperature θ to zero. We will comment further on the role of the $E^{1/3}$-ageostrophic layer in §6. For the moment we simply note that, since only one boundary condition at $x=0$ is required for solutions of the $E^{2/9}$-convection layer equation (3.18), matching to solutions which tend to zero across the thinner $E^{1/3}$-ageostrophic layer, leads to the boundary condition $\mathscr{W}(0) \approx 0$ on the tangent cylinder. More precisely, the error is proportional to the ratio of the boundary-layer length scales and so $\mathscr{W}(0) = O(E^{1/3}/E^{2/9}) = O(E^{1/9})$. The solution of the Airy equation (3.18), which satisfies the zero boundary condition, is

$$\mathscr{W}(x) = \mathrm{Ai}\left(-\lambda x + \rho\right), \qquad (3.20)$$

where ρ is a zero of the Airy function $\mathrm{Ai}(\rho)=0$. In addition, we have

$$\lambda = \left[-2\left(\frac{\partial\omega}{\partial s}\right)_c \Big/ \left(\frac{\partial^2\omega}{\partial k^2}\right)_c\right]^{1/3}, \qquad (3.21a)$$

where the root taken is that which achieves the correct matching at large x. That determines the requirement that

$$\mathrm{Re}\{\lambda\} < 0, \qquad |\mathrm{Im}\{\lambda\}| < \pi/3. \qquad (3.21b)$$

We note in passing that it is the failure of (3.18) to possess solutions that decay as x tends to both $+$ and $-\infty$ that necessitates the more complicated theory developed in JSM for the internal modes that occur in the full sphere.

The set of zeros determines the spectrum of our eigenvalue problem. Since the onset of instability corresponds to the smallest zero (in magnitude) $\rho = \rho_0 \approx -2.338$, that is the one to which we restrict attention. Accordingly, (3.18) is solved by (3.20)

when

$$\left(\frac{\partial\omega}{\partial\mathscr{R}}\right)_c \mathscr{R}_1 - \left[\omega_1 - \left(\frac{\partial\omega}{\partial m}\right)_c m_1\right] = \frac{\rho_0\lambda^2}{2}\left(\frac{\partial^2\omega}{\partial k^2}\right)_c \equiv -\frac{\rho_0}{2\lambda}\left(\frac{\partial\omega}{\partial s}\right)_c, \qquad (3.22a)$$

where use has been made of (3.21a). The real and imaginary parts determine the solutions

$$\mathscr{R}_1 = -\frac{\rho_0}{2}\operatorname{Im}\left\{\frac{1}{\lambda}\left(\frac{\partial\omega}{\partial s}\right)_c\right\}\bigg/\operatorname{Im}\left\{\left(\frac{\partial\omega}{\partial\mathscr{R}}\right)_c\right\}, \qquad (3.22b)$$

$$\omega_1^{\mathrm{gv}} \equiv \omega_1 - \left(\frac{\partial\omega}{\partial m}\right)_c m_1 = \mathscr{R}_1\operatorname{Re}\left\{\left(\frac{\partial\omega}{\partial\mathscr{R}}\right)_c\right\} + \rho_0\operatorname{Re}\left\{\frac{1}{\lambda}\left(\frac{\partial\omega}{\partial s}\right)_c\right\}, \qquad (3.22c)$$

where, since $(\partial\omega/\partial m)_c$ is real, the values of ω_1 and m_1 cannot be determined independently; only ω_1^{gv} is fixed.

In view of the indeterminacy of the frequency corrections, we introduce the Doppler-shifted frequency

$$\Omega^{\mathrm{gv}} \equiv E^{-2/3}\omega^{\mathrm{gv}} = \Omega - E^{-1/3}\left(\frac{\partial\omega}{\partial m}\right)_c M, \qquad (3.23a)$$

as measured in the frame rotating at the group angular velocity $(\partial\Omega/\partial M)_c$. It has the asymptotic expansion

$$\omega^{\mathrm{gv}} = \omega_c^{\mathrm{gv}} + E^{2/9}\omega_1^{\mathrm{gv}} + \cdots, \qquad (3.23b)$$

where, of course, we define $\omega_c^{\mathrm{gv}} \equiv \omega_c - (\partial\omega/\partial m)_c m_c$.

3.3 *Rigid boundaries*

The asymptotic analysis set up above and all statements about ω and its partial derivatives pertain to the solution of the stress-free boundary eigenvalue problem posed by (3.11) and (3.12a), which determines $\omega = \omega^{\mathrm{SF}}$ (see (3.13b)).

For the rigid (no-slip) boundary case, we continue to define the critical values of all parameters and their partial derivatives by the lowest-order solution (identified by the subscript c) of the stress-free problem. The higher-order corrections $O(E^{2/9})$ are given in part by the stress-free values above, but we add to them the $O(E^{1/6})$ Ekman layer corrections triggered by the non-zero complex value of

$$\omega_{1c}^{\mathrm{NS}} \equiv \omega_1^{\mathrm{NS}}(\eta, 0, m_c, \mathscr{R}_c). \qquad (3.24)$$

Accordingly, (3.19) is replaced by

$$R = E^{-4/3}\left(\mathscr{R}_c + E^{2/9}\mathscr{R}_1 + \cdots + E^{1/6}\widetilde{\mathscr{R}}\right), \qquad (3.25a)$$

$$\Omega = E^{-2/3}\left(\omega_c + E^{2/9}\omega_1 + \cdots + E^{1/6}\widetilde{\omega}\right), \qquad (3.25b)$$

$$M = E^{-1/3}\left(m_c + E^{2/9}m_1 + \cdots + E^{1/6}\widetilde{m}\right). \qquad (3.25c)$$

The corrections, like (3.22) above, satisfy

$$\left(\frac{\partial\omega}{\partial\mathscr{R}}\right)_c\widetilde{\mathscr{R}} - \left[\widetilde{\omega} - \left(\frac{\partial\omega}{\partial m}\right)_c\widetilde{m}\right] = -\omega_{1c}^{\mathrm{NS}}. \qquad (3.26a)$$

The real and imaginary parts determine the solutions

$$\widetilde{\mathscr{R}} = -\operatorname{Im}\left\{\omega_{1c}^{\mathrm{NS}}\right\}\bigg/\operatorname{Im}\left\{\left(\frac{\partial\omega}{\partial\mathscr{R}}\right)_c\right\}, \qquad (3.26b)$$

$$\widetilde{\omega}^{\mathrm{gv}} \equiv \widetilde{\omega} - \left(\frac{\partial \omega}{\partial m}\right)_c \widetilde{m} = \widetilde{\mathscr{R}} \operatorname{Re}\left\{\left(\frac{\partial \omega}{\partial \mathscr{R}}\right)_c\right\} + \operatorname{Re}\left\{\omega_{1c}^{\mathrm{NS}}\right\}, \qquad (3.26c)$$

and the Doppler-shifted frequency

$$\omega^{\mathrm{gv}} = \omega_c^{\mathrm{gv}} + E^{2/9}\omega_1^{\mathrm{gv}} + \cdots + E^{1/6}\widetilde{\omega}^{\mathrm{gv}}. \qquad (3.27)$$

4. Uniform distribution of internal heat sources: $\mathcal{Q} = 1$

4.1 *Small inner core: aspect ratio* $\eta = 0.35$

For the case of a sufficiently small inner core, the asymptotic solution is identical to the full sphere case investigated by JSM and applies to the aspect ratio $\eta = 0.35$ considered here. As the Ekman number decreases, the convection concentrates on the cylinder $s = s_M$ (see (1.2c)) and we obtain an interior mode uninfluenced by the presence of the inner core. In the small Ekman number asymptotic limit, the onset of convection is characterized by the asymptotic expansions

$$R = E^{-4/3}\left(\mathscr{R}_c + E^{1/3}\mathscr{R}_1 + \cdots + E^{1/6}\widetilde{\mathscr{R}}\right), \qquad (4.1a)$$

$$\Omega = E^{-2/3}\left(\omega_c + E^{1/3}\omega_1 + \cdots + E^{1/6}\widetilde{\omega}\right), \qquad (4.1b)$$

$$M = E^{-1/3}\left(m_c + E^{1/3}m_1 + \cdots + E^{1/6}\widetilde{m}\right), \qquad (4.1c)$$

as in (3.25) above except that the lowest-order corrections to the stress-free boundary-value problem are $O(E^{1/3})$ rather than the smaller $O(E^{2/9})$ appropriate to the tangent cylinder modes. We again introduce the Doppler-shifted frequency (3.23), but its expansion, which replaces (3.27), is

$$\omega^{\mathrm{gv}} = \omega_c^{\mathrm{gv}} + E^{1/3}\omega_1^{\mathrm{gv}} + \cdots + E^{1/6}\widetilde{\omega}^{\mathrm{gv}}. \qquad (4.2)$$

The rigid-boundary corrections are determined as for the tangent cylinder modes by (3.26). We checked that all our critical values agreed with JSM and noted in particular that

$$\mathscr{R}_c \approx 4.1173, \quad \omega_c \approx 0.4715, \quad m_c \approx 0.3029, \quad s_c \approx 0.5342 - 0.09667\,\mathrm{i}, \qquad (4.3a)$$

$$(\partial\omega/\partial\mathscr{R})_c \approx 0.03658 + 0.1062\,\mathrm{i}, \qquad (\partial\omega/\partial m)_c \approx 0.5186. \qquad (4.3b, c)$$

We also determined

$$\omega_{1c}^{\mathrm{NS}} \equiv \omega_1^{\mathrm{NS}}(s_c, 0, m_c, \mathscr{R}_c) = -0.74931 - 0.01281\,\mathrm{i} \qquad (4.3d)$$

by the perturbation method explained towards the end of § 3.1 below (3.13c). It is important to appreciate that the entire perturbation calculation is undertaken with the critical values, despite the fact that the position s_c is complex and motion is localized near s_M. Though counterintuitive, the procedure must be implemented because the eigenvalue problem is resolved at this complex location s_c. In this way, we determine the $O(E^{1/6})$ rigid-boundary corrections in (4.1).

In summary, JSM's full sphere parameter values together with our rigid-boundary corrections are

$$\left.\begin{array}{lll} \mathscr{R}_c \approx 4.1173, & \mathscr{R}_1 \approx 17.7815, & \widetilde{\mathscr{R}} \approx 0.1206, \\ \omega_c^{\mathrm{gv}} \approx 0.3144, & \omega_1^{\mathrm{gv}} \approx -0.6089, & \widetilde{\omega}^{\mathrm{gv}} \approx -0.7449. \end{array}\right\} \qquad (4.4)$$

The critical values obtained from numerically integrating the complete set of PDEs that govern our problem are summarized in table 1, where they are identified by

E	10^{-5}	$10^{-5.5}$	10^{-6}	$10^{-6.5}$	10^{-7}
			Leading-order asymptotic results		
R_c	1.9111×10^7	8.8705×10^7	4.1173×10^8	1.9111×10^9	8.8705×10^9
Ω_c	1015.816	2188.510	4715.002	10158.164	21885.102
M_c	14.059	20.636	30.290	44.460	65.258
			Stress-free boundary conditions		
			Numerical results		
R_N	2.1007×10^7	9.4610×10^7	4.3002×10^8	1.9684×10^9	9.0532×10^9
Ω_N	961.920	2121.810	4635.160	10028.470	21722.451
M_N	13	20	30	44	65
			Asymptotic results		
R_A	2.0889×10^7	9.4328×10^7	4.2951×10^8	1.9673×10^9	9.0483×10^9
$\Omega_A^\dagger$	962.053	2124.543	4639.072	10033.802	21725.109
			No-slip boundary conditions		
			Numerical results		
R_N	2.0720×10^7	9.3630×10^7	4.2700×10^8	1.9598×10^9	9.0264×10^9
Ω_N	731.180	1704.860	3885.980	8702.013	19357.031
M_N	13	20	30	44	65
			Asymptotic results		
R_A	2.0971×10^7	9.4642×10^7	4.3072×10^8	1.9719×10^9	9.0660×10^9
$\Omega_A^\dagger$	726.496	1705.656	3894.175	8709.165	19369.535

TABLE 1. The values of R, Ω and M for the case of internal heating with small inner core $\eta = 0.35$. The subscripts c, N and A identify the critical values (see (4.3a)), the results of the complete solution of the governing PDEs and the full asymptotic solution, respectively. That means $R_c = \mathscr{R}_c/E^{4/3}$, $R_A = (\mathscr{R}_c + E^{1/3}\mathscr{R}_1)/E^{4/3}$ (stress-free) and $R_A = (\mathscr{R}_c + E^{1/3}\mathscr{R}_1 + E^{1/6}\hat{\mathscr{R}})/E^{4/3}$ (no-slip). Similar expansions determine $\Omega_A^\dagger$ (see (4.6)), which is the asymptotic value of Ω evaluated with $M = M_N$. Note that the non-integer values of M_c reflect our asymptotic assumption that under minimization, m is regarded as a continuous rather than a discrete variable.

the subscript N. For comparison, we first list the leading-order asymptotic results $R_c = \mathscr{R}_c/E^{4/3}$, $\Omega_c = \omega_c/E^{2/3}$ and $M_c = m_c/E^{1/3}$. For a tighter comparison we also list the higher-order asymptotic results $R \approx (\mathscr{R}_c + E^{1/3}\mathscr{R}_1)/E^{4/3}$ in the case of stress-free boundaries and $R \approx (\mathscr{R}_c + E^{1/3}\mathscr{R}_1 + E^{1/6}\hat{\mathscr{R}})/E^{4/3}$ in the case of rigid boundaries with the no-slip boundary condition. Since the asymptotic results, identified by the subscript A in table 1, do not determine the corrections to M and Ω independently, we fix M by the numerical solution M_N. Accordingly, we list the asymptotic value of Ω based on $M = M_N$, namely

$$\Omega^\dagger = \Omega^{\mathrm{gv}} + E^{-1/3}\left(\frac{\partial \omega}{\partial m}\right)_c M_N, \qquad (4.5)$$

where $\Omega^{\mathrm{gv}} = \omega^{\mathrm{gv}}/E^{2/3}$ is determined by the formula (3.23) and the parameter values (4.3) and (4.4).

Though table 1 provides a means of comparing the asymptotic predictions with the numerical results, an alternative and perhaps more immediate comparison is portrayed in figure 1, where we plot $\mathscr{R}$ and ω^{gv} versus E. It is important to appreciate that at small Ekman number, the no-slip corrections are an order of magnitude larger
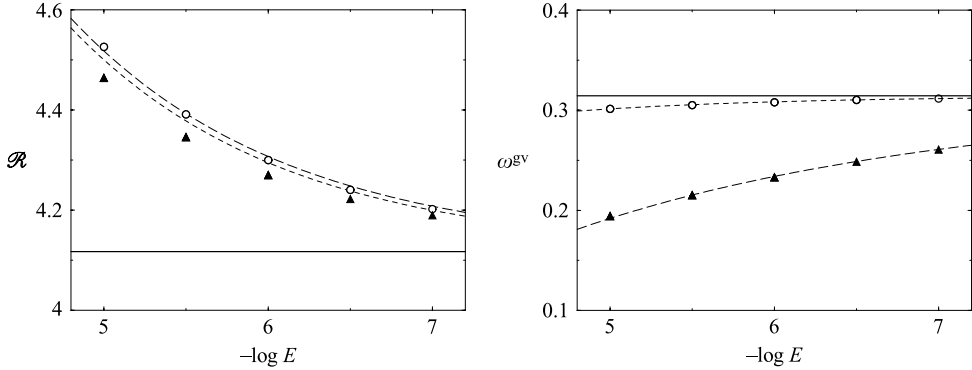
FIGURE 1. The interior mode for the case of internal heating with small inner core $\eta = 0.35$. Plots of the scaled Rayleigh number $\mathcal{R} \equiv R/E^{4/3}$ and the scaled Doppler shifted frequency ω^{gv} [see (3.23a)] *vs.* Ekman number. The full numerical results $\mathcal{R}_N$ and ω_N^{gv} determined from the data in table 1 are identified for the case of stress-free boundaries by the open circles and for the case of no-slip boundaries by the solid triangles. The asymptotic results $\mathcal{R}_A = \mathcal{R}_c + E^{1/3}\mathcal{R}_1$ and $\omega_A^{\mathrm{gv}} = \omega_c^{\mathrm{gv}} + E^{1/3}\omega_1^{\mathrm{gv}}$ for stress-free boundaries are denoted by the short dashed lines; the asymptotic results $\mathcal{R}_A = \mathcal{R}_c + E^{1/3}\mathcal{R}_1 + E^{1/6}\widetilde{\mathcal{R}}$ and $\omega_A^{\mathrm{gv}} = \omega_c^{\mathrm{gv}} + E^{1/3}\omega_1^{\mathrm{gv}} + E^{1/6}\widetilde{\omega}^{\mathrm{gv}}$ for no-slip boundaries are denoted by the long dashed lines. The critical values $\mathcal{R}_c$ and ω_c^{gv}, to which they asymptote, are given by the continuous horizontal straight lines.

E	10^{-5}	$10^{-5.5}$	10^{-6}	$10^{-6.5}$	10^{-7}	$\mathcal{R} = \mathcal{R}_A$
	$\mathcal{R} = \mathcal{R}_N,$		$\omega^{\mathrm{gv}} = \omega_N^{\mathrm{gv}}$			$\omega^{\mathrm{gv}} = \omega_A^{\mathrm{gv}}$
		Stress-free boundary conditions				
$(\mathcal{R}_{\mathrm{SF}} - \mathcal{R}_c)/E^{1/3}$	18.962	18.674	18.290	18.125	18.274	17.781
$(\omega_{\mathrm{SF}}^{\mathrm{gv}} - \omega_c^{\mathrm{gv}})/E^{1/3}$	-0.612	-0.649	-0.648	-0.645	-0.621	-0.609
		No-Slip boundary conditions				
$(\mathcal{R}_{\mathrm{NS}} - \mathcal{R}_{\mathrm{SF}})/E^{1/6}$	-0.421	-0.375	-0.302	-0.224	-0.182	0.121
$(\omega_{\mathrm{NS}}^{\mathrm{gv}} - \omega_{\mathrm{SF}}^{\mathrm{gv}})/E^{1/6}$	-0.730	-0.741	-0.749	-0.746	-0.748	-0.745

TABLE 2. The case of internal heating with small inner core $\eta = 0.35$ as in table 1. In the case of the stress-free entries, the differences between the numerically computed values of $\mathcal{R}_{\mathrm{SF}} = E^{4/3}R_N$ and $\omega_{\mathrm{SF}}^{\mathrm{gv}} = E^{2/3}\Omega_N - E^{1/3}(\partial\omega/\partial m)_c M_N$ and their leading-order asymptotic representations are given and compared with the predicted asymptotic differences $\mathcal{R}_1$ and ω_1^{gv}. In the case of the no-slip entries, the differences between their numerically computed values of $\mathcal{R}_{\mathrm{NS}}$ and $\omega_{\mathrm{NS}}^{\mathrm{gv}}$ and the corresponding stress-free values are given and compared with the predicted asymptotic differences $\widetilde{\mathcal{R}}$ and $\widetilde{\omega}^{\mathrm{gv}}$ given in the final column.

than the stress-free corrections. This is evident in the plots of the Doppler-shifted frequency ω^{gv}, where comparison with the numerical results is excellent. That is not the case with the Rayleigh number plots, where quantitatively the rigid boundary corrections appear to be small. This is a consequence of the fact that the numerical value of $\widetilde{\mathcal{R}}$ is relatively small in comparison with $\mathcal{R}_1$. It means that we would need to go to much smaller values of E before reaching the relative sizes indicated by the asymptotics. Further insight into the accuracy of the results may be seen from the alternative comparisons in table 2, in which the poor convergence of $(\mathcal{R}_{\mathrm{NS}} - \mathcal{R}_{\mathrm{SF}})/E^{1/6}$ (see the table caption) to $\widetilde{\mathcal{R}}$ is accounted for as above by its small size. This feature should be compared with Zhang & Jones (1993) small inner core ($\eta = 0.4$) results

reported for moderate Ekman number ($E = 10^{-4}$). Their figure 3 plots the critical Rayleigh number for those parameter values as a function of the Prandtl number P. It shows that $\mathscr{R}_{NS} - \mathscr{R}_{SF}$ is positive for small P, negative for large P with the value zero achieved for P roughly (but just less than) unity. Those results are totally consistent with the small negative value of $(\mathscr{R}_{NS} - \mathscr{R}_{SF})/E^{1/6}$ determined by our full numerics.

Before continuing to the tangent cylinder modes, it is helpful to recall the nature of the realized interior modes. As JSM explained, the radial wavenumber $k(s)/E^{1/3}$ in the WKB-solution (3.3) is determined as a complex function of s by the dispersion relation $\omega(s, k, m_c, \mathscr{R}_c) = \omega_c$. The solution is localized in the vicinity of $s = s_M \approx 0.5915$ (see (1.2c)), where $\text{Im}\{k(s_M)\} = 0$. There, the amplitude of the solution is proportional to

$$\mathscr{K}(s) = \exp\left[i k_M \frac{s - s_M}{E^{1/3}} + \frac{i k'_M}{2} \frac{(s - s_M)^2}{E^{1/3}} \right], \tag{4.6}$$

where $k_M = k(s_M) \approx -0.3486$ and $k'_M = \text{d}k/\text{d}s(s_M) \approx -1.595 + 1.710\,\text{i}$. It is important to appreciate that it describes a wave on the short length scale $O(E^{1/3})$, but modulated in amplitude under a Gaussian envelope of relatively broad width $O(E^{1/6})$. The fact that both the azimuthal and radial wavenumbers m_c/s_M and k_M are of the same order of magnitude means that the convection rolls are tilted at a finite angle $\tan^{-1}(-s_M k_M/m_c) \approx 34.2°$ to meridional planes. Furthermore, the number of radial oscillations under the envelope increases with decreasing E. These are features that we will contrast with the nature of the tangent cylinder modes.

4.2. *Large inner core: aspect ratio $\eta = 0.65$*

When the inner core is sufficiently large, the critical mode is no longer an interior mode, but confines itself to the tangent cylinder, as we explained in §3. We take, as an illustrative example, the case of the core aspect ratio $\eta = 0.65$.

Our minimization of $\mathscr{R}$ determines the critical values

$$\mathscr{R}_c \approx 3.6732\,, \qquad \omega_c \approx 0.5596\,, \qquad m_c \approx 0.4518\,. \tag{4.7}$$

The partial derivatives of the frequency at these critical values required for the higher-order theory are

$$(\partial\omega/\partial\mathscr{R})_c \approx -0.0305 + 0.1973\,\text{i}\,, \qquad (\partial\omega/\partial m)_c \approx -1.7351\,, \tag{4.8a,b}$$

$$(\partial\omega/\partial s)_c \approx 3.0614 - 0.8457\,\text{i}\,, \qquad (\partial^2\omega/\partial k^2)_c \approx -2.1820 - 1.4555\,\text{i}\,. \tag{4.8c,d}$$

We also determine

$$\omega_{1c}^{NS} = -1.37463 - 0.46876\,\text{i}\,. \tag{4.8e}$$

We use the partial derivatives (4.8c, d) to calculate λ defined by (3.21). It is

$$\lambda = -0.97221 - 0.92639\,\text{i}\,. \tag{4.9}$$

In turn, using (3.22), (3.26) and (4.8a, b, e) we obtain

$$\left.\begin{aligned}
\mathscr{R}_c &\approx 3.6732\,, & \mathscr{R}_1 &\approx 24.03908\,, & \widetilde{\mathscr{R}} &\approx 2.37555\,, \\
\omega_c^{gv} &\approx 1.34352\,, & \omega_1^{gv} &\approx 2.10892\,, & \widetilde{\omega}^{gv} &\approx -1.44718\,.
\end{aligned}\right\} \tag{4.10}$$

These values are used to determine the asymptotic results given in tables 3 and 4, as well as the asymptotic curves in figure 2. Comparison with the numerical results is favourable as it was for the small inner core case discussed in the previous subsection, but with the same type of discrepancies again evident in the values of the no-slip Rayleigh numbers.

E	10^{-5}	$10^{-5.5}$	10^{-6}	$10^{-6.5}$	10^{-7}
		Leading-order asymptotic results			
R_c	1.7049×10^7	7.9136×10^7	3.6732×10^8	1.7049×10^9	7.9136×10^9
Ω_c	1205.687	2597.573	5596.302	12056.867	25975.734
M_c	20.973	30.784	45.184	66.321	97.346
		Stress-free boundary conditions			
		Numerical results			
R_N	2.5851×10^7	1.0958×10^8	4.7487×10^8	2.0899×10^9	9.3024×10^9
Ω_N	1271.817	2756.021	5901.283	12577.062	27012.674
M_N	24	34	49	71	102
		Asymptotic results			
R_A	2.5689×10^7	1.1018×10^8	4.7890×10^8	2.1059×10^9	9.3547×10^9
$\Omega_A^\dagger$	1313.657	2804.168	5913.063	12498.104	26959.770
		No-slip boundary conditions			
		Numerical results			
R_N	2.5740×10^7	1.0985×10^8	4.7910×10^8	2.1176×10^9	9.4472×10^9
Ω_N	860.080	2040.988	4702.119	10449.477	23151.811
M_N	24	34	48	70	101
		Asymptotic results			
R_A	2.7307×10^7	1.1639×10^8	5.0266×10^8	2.1970×10^9	9.7035×10^9
$\Omega_A^\dagger$	856.015	1990.353	4639.384	10179.275	22757.172

TABLE 3. As in table 1, but for the case of internal heating with large inner core $\eta = 0.65$. The asymptotic expansions, however, are based on (3.25) rather than (4.1).

E	10^{-5}	$10^{-5.5}$	10^{-6}	$10^{-6.5}$	10^{-7}	$\mathscr{R} = \mathscr{R}_A$
		$\mathscr{R} = \mathscr{R}_N$,	$\omega^{gv} = \omega_N^{gv}$			$\omega^{gv} = \omega_A^{gv}$
		Stress-free boundary conditions				
$(\mathscr{R}_{SF} - \mathscr{R}_c)/E^{2/9}$	24.491	23.574	23.171	23.078	23.166	24.039
$(\omega_{SF}^{gv} - \omega_c^{gv})/E^{2/9}$	1.858	1.936	2.084	2.211	2.150	2.109
		No-slip boundary conditions				
$(\mathscr{R}_{NS} - \mathscr{R}_{SF})/E^{1/6}$	−0.163	0.102	0.423	0.723	0.987	2.376
$(\omega_{NS}^{gv} - \omega_{SF}^{gv})/E^{1/6}$	−1.302	−1.272	−1.373	−1.340	−1.339	−1.447

TABLE 4. As in table 2, but for the case of internal heating with large inner core $\eta = 0.65$. As noted in table 3, the asymptotic expansions are different.

The eigenfunctions for the numerical and asymptotic results are compared in figure 3. To that end, we plot the equatorial values on $z = 0$ of the complex temperature θ, the radial and azimuthal velocities (v_s, v_ϕ) (see (3.9)). According to the definition (3.2) and the scalings (3.9), we have from (3.17) the asymptotic relations

$$\theta \approx \widehat{\theta}_c(\eta, 0) \, \mathscr{W}(x) \, \mathscr{E}(\phi, t), \tag{4.11a}$$

$$v_s \approx \mathrm{i}(m/\eta) \widehat{\psi}_c(\eta, 0) \, \mathscr{W}(x) \, \mathscr{E}(\phi, t), \tag{4.11b}$$

$$v_\phi \approx - E^{1/9} \widehat{\psi}_c(\eta, 0) \, \mathrm{d}\mathscr{W}/\mathrm{d}x(x) \, \mathscr{E}(\phi, t), \tag{4.11c}$$
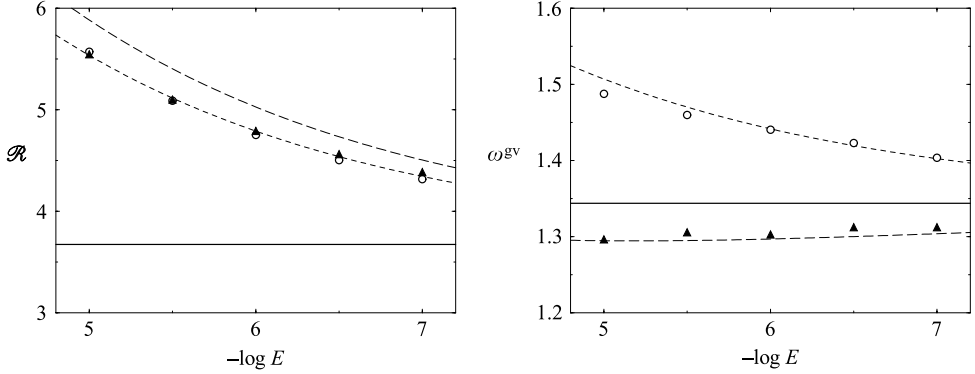
FIGURE 2. The tangent cylinder mode for the case of internal heating with large inner core $\eta = 0.65$; plots as in figure 1, except that the asymptotic expansions used for the analytic results are based on (3.25) rather than (4.1).

where, as usual, $\mathscr{E} = \exp[\mathrm{i}(M\phi - \Omega t)]$ and $x = (s - \eta)/E^{2/9}$ is the boundary-layer coordinate. In terms of our Airy function solution (3.20), these become

$$\theta \approx \widehat{\theta}_c(\eta, 0)\mathrm{Ai}(-\lambda x + \rho_0)\,\mathscr{E}(\phi, t), \qquad (4.12a)$$

$$v_s \approx \mathrm{i}(m_c/\eta)\widehat{\psi}_c(\eta, 0)\,\mathrm{Ai}(-\lambda x + \rho_0)\,\mathscr{E}(\phi, t), \qquad (4.12b)$$

$$v_\phi \approx E^{1/9}\widehat{\psi}_c(\eta, 0)\,\lambda\,\mathrm{Ai}'(-\lambda x + \rho_0)\,\mathscr{E}(\phi, t), \qquad (4.12c)$$

where Ai' is the derivative of the Airy function. Here, $\widehat{\psi}_c(s, z)$ and $\widehat{\theta}_c(s, z)$ are related to $\widehat{w}_c(s, z)$ by (3.10a–c) and in particular we have

$$\left[(m_c^2/\eta^2) - \mathrm{i}P\omega_c\right]\widehat{\theta}_c(\eta, 0) \approx \mathrm{i}\mathscr{Q}_i m_c\widehat{\psi}_c(\eta, 0), \qquad (4.13)$$

where $\mathscr{Q}_i = 1$. Of some interest is the radial derivative of v_ϕ determined from (4.12c), namely,

$$\partial v_\phi/\partial s \approx E^{-1/9}\widehat{\psi}_c(\eta, 0)\,\lambda^2(\lambda x - \rho_0)\,\mathrm{Ai}(-\lambda x + \rho_0)\,\mathscr{E}(\phi, t). \qquad (4.14)$$

So from the asymptotic results (4.12) and (4.14), we see that θ, v_s and $E^{1/9}\partial v_\phi/\partial s$ all vanish at lowest order on the equator $z = 0$ of the tangent cylinder $x = 0$, because $\mathrm{Ai}(\rho_0) = 0$. These asymptotic predictions agree with the numerics; though in the case of $E^{1/9}\partial v_\phi/\partial s$ only just outside thinner boundary layers that our asymptotics is unable to resolve. This is important because it provides an independent numerical verification of the choice of boundary condition $\mathscr{W}(0) \approx 0$ used in constructing our asymptotic solution.

In the plots we normalize the complex value of $\widehat{\psi}_c(\eta, 0)$ via the characteristics of v_s. Specifically, we fix the amplitude by demanding that the maximum of $|v_s|$ is unity for all the numerical and asymptotic cases. The resulting asymptotic values of $|\theta|$, $|v_s|$ and $|v_\phi|/E^{1/9}$ plotted versus the boundary-layer coordinate x are compared with the numerical results for decreasing Ekman number in the graphs in the left-hand column of figure 3. In the right-hand column of figure 3 only one value of the Ekman number, namely $E = 10^{-7}$, is employed for the numerics. There, in addition to magnitudes, the real parts of θ, v_s and $v_\phi/E^{1/9}$ are illustrated. The phase for the numerics was chosen arbitrarily, but having selected it, the phase for the asymptotic results is fixed by demanding that the first zero of the plotted $\mathrm{Re}\{v_s\}$ for both the
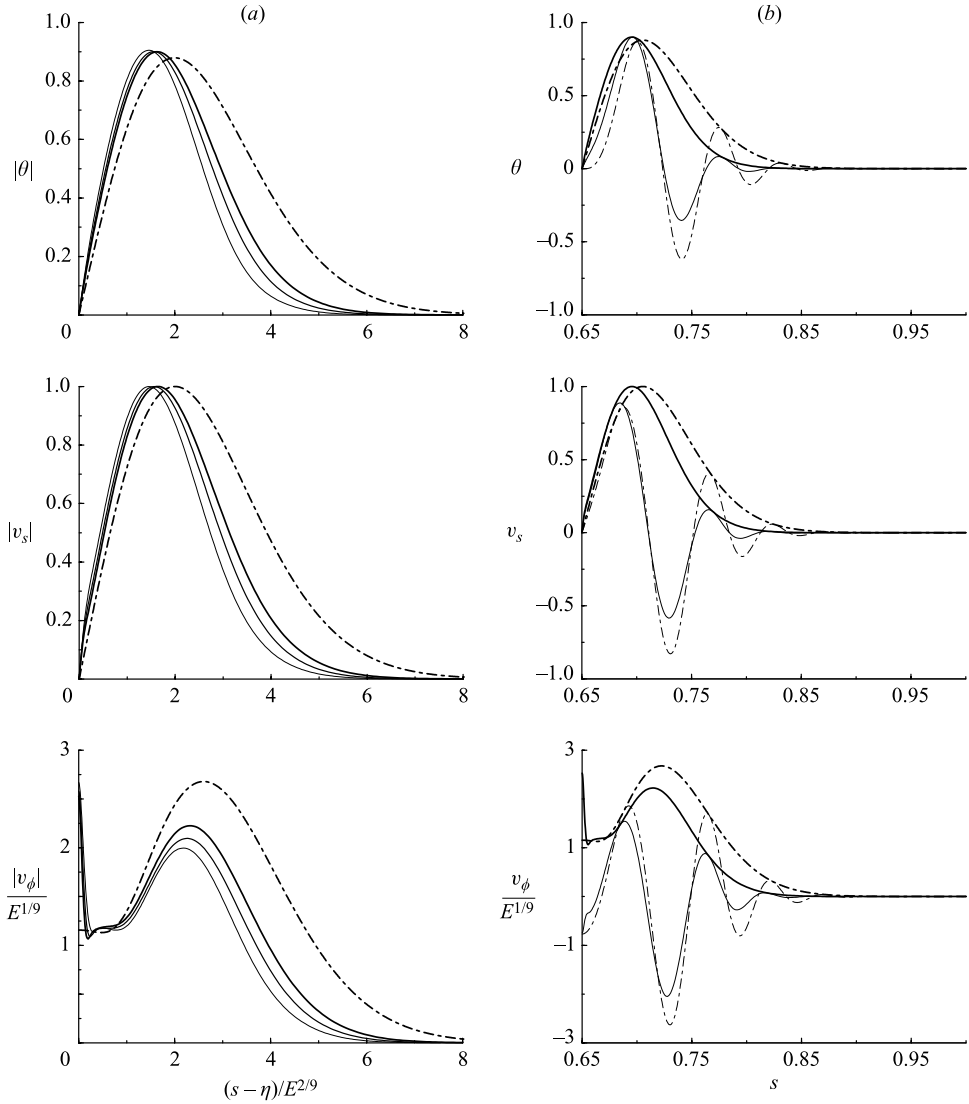
FIGURE 3. The tangent cylinder eigenfunctions θ, v_s and $v_\phi/E^{1/9}$ in the equatorial plane $z = 0$ for the case of internal heating and stress-free boundaries with large inner core $\eta = 0.65$. (a) The numerical results for $|\theta|$, $|v_s|$ and $|v_\phi|/E^{1/9}$ at $E = 10^{-6}$, $10^{-6.5}$ and 10^{-7} are plotted vs. $x = (s - \eta)/E^{2/9}$ and indicated by the continuous lines thickening with decreasing Ekman number. The leading-order asymptotic results (dot-dashed lines) given by (4.12) involve the Airy function (θ, v_s) and its derivative ($v_\phi/E^{1/9}$). (b) The real parts (thin lines) and moduli (thick lines) for the numerical results at $E = 10^{-7}$ (continuous lines) and asymptotic results (dot-dashed lines) plotted vs. s.

numerical and asymptotic solutions coincide. That essentially determines the phase of $\widehat{\psi}_c(\eta, 0)$ in (4.12b) (or more precisely $\widehat{\psi}_c(\eta, 0)\mathscr{E}(\phi, t)$) which in turn fixes the phases of θ and $v_\phi/E^{1/9}$ in (4.12a, c) via (4.13). Each of the graphs in this right-hand column is plotted versus the actual radial coordinate s in order to provide a quantitative picture of the thickness of the $E^{2/9}$-convection layer.

It should also be noted that from an asymptotic point of view, v_ϕ is small. Specifically, we have

$$v_\phi = O\left(E^{1/9} v_s\right). \tag{4.15}$$

Indeed, it is remarkable how well the asymptotics agrees with the numerics for this relatively small quantity, which we might expect to respond significantly to the presence of the thinner $E^{1/3}$-ageostrophic layer. We will discuss this issue more carefully in §6. We also note that the divergence of the numerics from the asymptotics as $x \downarrow 0$ reflects the fact that there are yet smaller boundary layers on the equator of the inner sphere that our asymptotics fails to capture.

Of course, our normalizations have been chosen to obtain the best agreement in figure 3 between the numerical and asymptotic results for v_s. Nevertheless, the numerical trend for the other quantities θ and $v_\phi/E^{1/9}$ towards the asymptotic predictions is most reassuring and we may reasonably suppose that the asymptotic results will eventually be reached at sufficiently small Ekman number. Convergence to the asymptotic limit is slow, because, though the smallest value of $E = 10^{-7}$ attained is truly small, the expansion parameter identified in (4.15) is $E^{1/9}$; this result is consistent with our estimation just below (3.20) that $\mathscr{W}(0) = O(E^{1/9})$. Accordingly, our $O(E^{1/9})$ errors are not actually small even when $E = 10^{-7}$ and neither is the $E^{2/9}$-convection layer width identified in the graphs portrayed in the right-hand column of figure 3. The latter observation is certainly cause for concern when comparing the eigenfunctions because the asymptotic solutions are determined by conditions at the tangent cylinder $s = \eta$ (see (4.12)) and do not take into account the actual conditions that prevail elsewhere $s > \eta$. Such eigenfunction discrepancies are clearly evident in the case of the differential heating, as we will explain in the next section.

From a physical point of view, the fact that the wavenumber k (see (3.16b)) of the WKB-solution tends to zero as $s \downarrow \eta$ means that the convective rolls are normal to the inner boundary. They then bend to a finite positive angle of inclination with the meridional planes over the radial length scale $O(E^{2/9})$, as illustrated by the contour plots on the left-hand side of figure 4. There, the numerically computed axial vorticity is plotted in the upper figure, while the corresponding asymptotic results at the same azimuthal wavenumber M are plotted below. The latter are proportional to the data for v_s illustrated in the right-hand column of figure 3. Compatible with numerical and asymptotic data for v_s on figure 3, the tilt angle of both sets of rolls is the same, whereas the radial extent of the numerically computed rolls is smaller than that predicted by the asymptotics. This may be explained by the fact that the assumptions made in the asymptotic calculation underestimate the actual inhibiting effect of the rapidly deceasing height $z = h(s)$ of the outer boundary, as s increases in the relatively thin shell $0.65 \leqslant s \leqslant 1$.

In the no-slip case, we have no asymptotic eigenfunctions except in as much as they are the same, correct to lowest order, as those for the stress-free case. Since our only asymptotic eigenfunctions do not take into account the no-slip boundary condition, we see no merit in comparing them with numerical results that do.

5. Differential heating: $\mathscr{Q} = 1/r^3$

In the case of differential heating, the temperature gradient increases very rapidly with decreasing r and so the convection always occurs on the tangent cylinder irrespective of the size of the inner core. In this section, we take, as an illustrative example, the aspect ratio $\eta = 0.35$ which closely resembles the geophysical value.
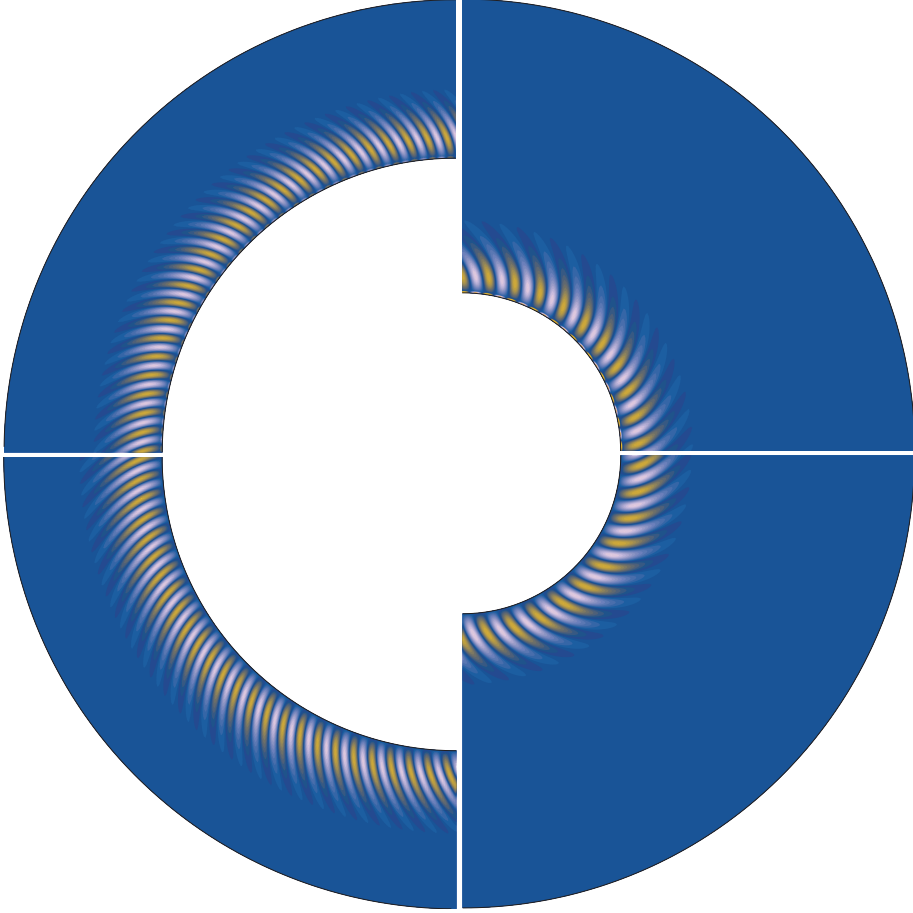
FIGURE 4. Comparison between equatorial cross-sections of the axial vorticity $\hat{z} \cdot \nabla \times \boldsymbol{u}$ in the full numerics for $E = 10^{-7}$ (top row), and the asymptotic eigenfunction ψ for the same Ekman number (bottom row). Internal heating with a large aspect ratio $\eta = 0.65$ ($M = 102$) is portrayed on the left; differential heating with aspect ratio $\eta = 0.35$ ($M = 41$) is portrayed on the right.

Since $\mathscr{F}$ in our ordinary differential equation (3.11) is now a function of z, the equation itself involves a first-order derivative in w, which prevents us from using a shooting method. Instead, a Thomas algorithm is used to solve it with an arbitrary inhomogeneous Neuman boundary condition.

Our minimization of $\mathscr{R}$ determines the critical values

$$\mathscr{R}_c \approx 0.285933, \qquad \omega_c \approx 0.337014, \qquad m_c \approx 0.179715. \tag{5.1}$$

The partial derivatives of the frequency at these critical values required for the higher-order theory are

$$(\partial\omega/\partial\mathscr{R})_c \approx -0.1220 + 1.3831\,\mathrm{i}, \qquad (\partial\omega/\partial m)_c \approx -2.2637, \tag{5.2a,b}$$

$$(\partial\omega/\partial s)_c \approx 2.5039 - 2.1466\,\mathrm{i}, \qquad (\partial^2\omega/\partial k^2)_c \approx -2.6568 - 1.1276\,\mathrm{i}. \tag{5.2c,d}$$

We also determine

$$\omega_{1c}^{\mathrm{NS}} = -0.69319 - 0.38592\,\mathrm{i}. \tag{5.2e}$$

E	10^{-5}	$10^{-5.5}$	10^{-6}	$10^{-6.5}$	10^{-7}
			Leading-order asymptotic results		
R_c	1.3272×10^6	6.1602×10^6	2.8593×10^7	1.3272×10^8	6.1602×10^8
Ω_c	726.075	1564.281	3370.141	7260.749	15642.812
M_c	8.342	12.244	17.971	26.379	38.718
			Stress-free boundary conditions		
			Numerical results		
R_N	3.0614×10^6	1.2099×10^7	4.9192×10^7	2.0511×10^8	8.7233×10^8
Ω_N	706.350	1535.850	3332.026	7182.550	15602.461
M_N	10	14	20	29	41
			Asymptotic results		
R_A	2.8224×10^6	1.1534×10^7	4.7905×10^7	2.0212×10^8	8.6544×10^8
$\Omega_A^\dagger$	646.705	1451.703	3174.950	6830.110	15264.679
			No-slip boundary conditions		
			Numerical results		
R_N	3.2400×10^6	1.2700×10^7	5.1525×10^7	2.1376×10^8	9.0545×10^8
Ω_N	550.170	1262.290	2845.529	6324.207	14018.014
M_N	9	13	19	28	40
			Asymptotic results		
R_A	3.0125×10^6	1.2262×10^7	5.0695×10^7	2.1281×10^8	9.0640×10^8
$\Omega_A^\dagger$	521.806	1196.975	2674.089	5869.156	13452.671

TABLE 5. As in table 3, but for the case of differential heating with core radius ratio $\eta = 0.35$.

E	10^{-5}	$10^{-5.5}$	10^{-6}	$10^{-6.5}$	10^{-7}	$\mathscr{R} = \mathscr{R}_A$
		$\mathscr{R} = \mathscr{R}_N$,	$\omega^{gv} = \omega_N^{gv}$			$\omega^{gv} = \omega_A^{gv}$
			Stress-free boundary conditions			
$(\mathscr{R}_{SF} - \mathscr{R}_c)/E^{2/9}$	4.826	4.598	4.438	4.340	4.275	4.161
$(\omega_{SF}^{gv} - \omega_c^{gv})/E^{2/9}$	0.926	0.871	0.907	1.024	0.830	0.569
			No-slip boundary conditions			
$(\mathscr{R}_{NS} - \mathscr{R}_{SF})/E^{1/6}$	0.262	0.230	0.233	0.226	0.226	0.279
$(\omega_{NS}^{gv} - \omega_{SF}^{gv})/E^{1/6}$	-0.826	-0.761	-0.713	-0.670	-0.655	-0.727

TABLE 6. As in table 4, but for the case of differential heating with core radius ratio $\eta = 0.35$.

We use the partial derivatives (5.2c, d) to determine λ defined by (3.21):

$$\lambda = -1.02657 - 0.82534\,\mathrm{i}\,. \tag{5.3}$$

In turn, using (3.22), (3.26) and (5.2), we obtain

$$\left.\begin{array}{lll} \mathscr{R}_c \approx 0.285933\,, & \mathscr{R}_1 \approx 4.16053\,, & \widetilde{\mathscr{R}} \approx 0.27902\,, \\ \omega_c^{gv} \approx 0.743835\,, & \omega_1^{gv} \approx 0.56878\,, & \widetilde{\omega}^{gv} \approx -0.72723\,. \end{array}\right\} \tag{5.4}$$

These values are used to determine the asymptotic results given in tables 5 and 6, as well as the asymptotic curves in figure 5. Comparison between the numerical results is again favourable, though the comparisons between the Doppler shifted frequencies ω^{gv} appear to require substantially smaller values of E than actually employed to obtain sharp agreement. Note, however, that there is a significant improvement in the
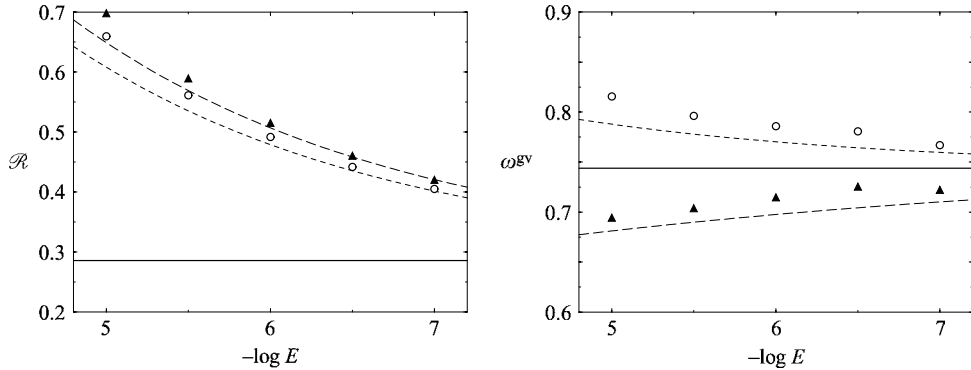
FIGURE 5. The tangent cylinder mode for the case of differential heating with aspect ratio $\eta = 0.35$; plots as in figure 2.

comparison of the no-slip values of the Rayleigh number, which may reflect the fact that the ratio $\widetilde{\mathscr{R}}/\mathscr{R}_1$, though still small, is much larger than the corresponding ratio determined by (4.4) for the internally heated case with the same core aspect ratio.

In figure 6, we compare the eigenfunctions of the numerical results and asymptotic results, which continue to be given by (4.12). In contrast to figure 3, we plot the buoyancy function $\theta/\mathscr{Q}$ (see (3.10a)) rather than θ because we believe that it more faithfully measures the role of the buoyancy forces. This distinction did not arise in the case of internal heating with $\mathscr{Q} = 1$ for then temperature θ and buoyancy $\theta/\mathscr{Q}$ are one and the same quantity. We do, however, portray the corresponding results for the temperature, albeit the scaled temperature $\theta/\mathscr{Q}_i$, in figure 7. We do that because the asymptotic solution plots for $\theta/\mathscr{Q}$ and $\theta/\mathscr{Q}_i$ on figures 6 and 7 coincide, since $\mathscr{Q} = \mathscr{Q}_i$ for all finite x in the limit $E \to 0$. So in a true asymptotic limit, the numerical plots of $\theta/\mathscr{Q}$ and $\theta/\mathscr{Q}_i$ should also coincide, which is evidently far from the case. The failure illustrated by this relatively simple comparison provides evidence that we are far from an asymptotic regime.

A little care must be taken in interpreting the amplitude and phase plot of the buoyancy $\theta/\mathscr{Q}$ versus the unstretched coordinate s figure 6(b)(i), as s is not a natural coordinate for the asymptotic solution. There numerical results are portrayed for the fixed Ekman number $E = 10^{-7}$, while the asymptotic solution plotted is $\theta/\mathscr{Q}_i = \eta^3\theta$ and not $\theta/\mathscr{Q} = s^3\theta$ suggested by the horizontal axis label s. Our convention is natural and maintains consistency with the amplitudes of both the numerical and asymptotic results plotted against boundary-layer coordinate $x = (s - r_i)/E^{2/9}$ in figure 6(a)(i). The graphs of the temperature on figure 7 correspond to those on figure 3 scaled by the factor $\mathscr{Q}_i = 1/\eta^3$. So had we plotted $\theta/\mathscr{Q} = s^3\theta$ in figure 6(b)(i), all the curves of both numerical and asymptotic results would simply be those portrayed figure 7(b) scaled by the factor s^3/η^3. We emphasize yet again the distinction between buoyancy and temperature does not arise in the case of internal heating with $\mathscr{Q} = 1$, for which plots of $\theta/\mathscr{Q}$ and $\theta/\mathscr{Q}_i$ double up as the single plot on figure 3.

In general terms, the comparisons of the numerical and asymptotic results for internal heating portrayed in figure 3 are sharper that those for differential heating in figure 6 (see also figure 4), suggesting that far smaller Ekman numbers are required in the latter case to reach an asymptotic limit. This slow convergence was also apparent in the Doppler shifted frequency plots in figure 5. An obvious weakness of the eigenfunctions is their failure to obtain good agreement with the wavelengths
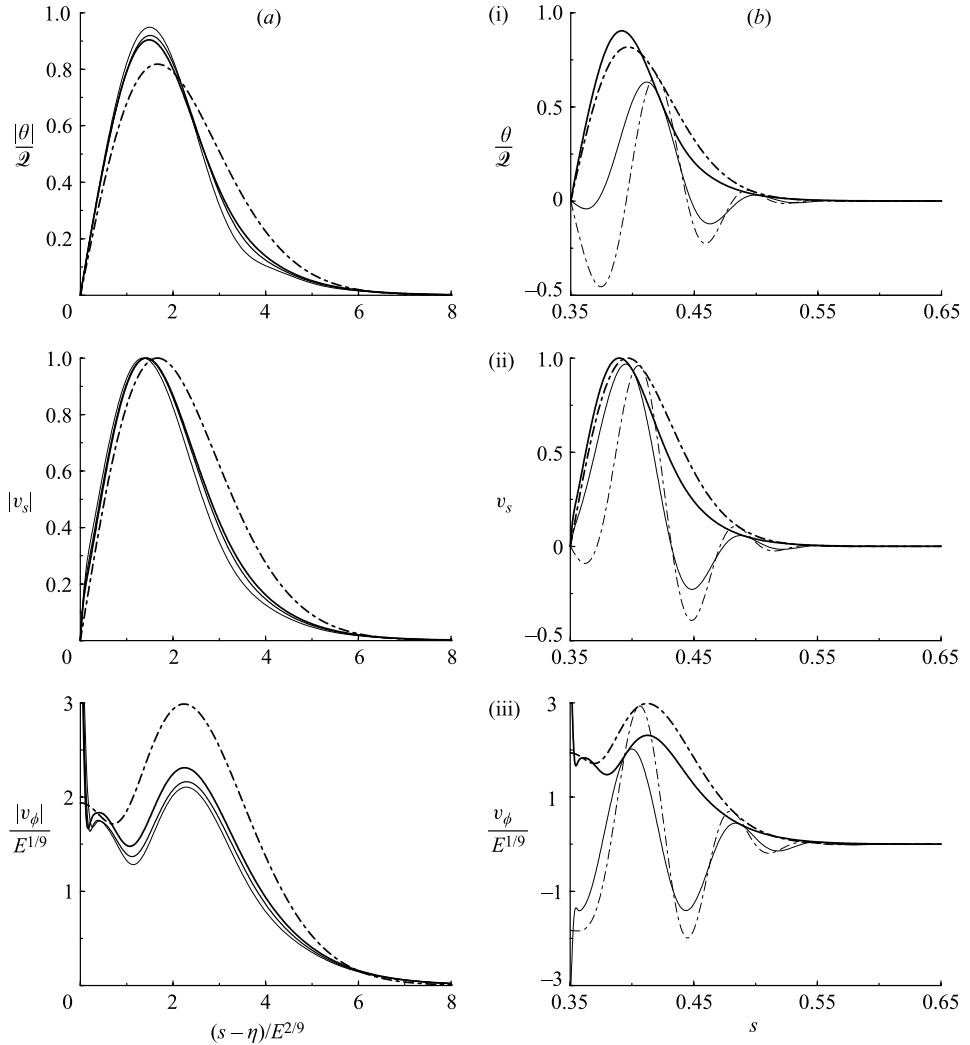
FIGURE 6. The tangent cylinder eigenfunctions for the case of differential heating and stress-free boundaries with aspect ratio $\eta = 0.35$; plots of v_s and $v_\phi/E^{1/9}$ as in figure 3. The θ plots are replaced by the buoyancy function $\theta/\mathcal{Q}$, which was equivalent to θ for the case of internal heating with $\mathcal{Q} = 1$, but now $\theta/\mathcal{Q} = s^3\theta$. Since the plots in (b)(i) are portayed using the unstretched variable s, we plot the asymptotic results for $\theta/\mathcal{Q}_i = \eta^3\theta$ to maintain consistency with the boundary-layer coordinate plot in (a)(i).

in figure 6(*b*). There seem to be two likely candidates for this weakness. One is that curvature effects (specifically their *s*-variations) are more pronounced for the smaller inner core $\eta = 0.35$. The other (and related) is the strong effect introduced by the variation of $\mathcal{Q}$ illustrated in the comparison between the plots of $\theta/\mathcal{Q}$ and $\theta/\mathcal{Q}_i$ in figures 6 and 7, which only identifies simple amplitude discrepancies. It is also clear that the *z*-structure characterized by $\widehat{w}(s, z)$ will also be sensitive to these *s*-dependencies with the consequence that much smaller values of E are required to achieve good phase agreement between the numerics and asymptotics.

Of course, we must be wary of the role of a thinner $E^{1/3}$-ageostrophic boundary layer, but we postpone commenting on that until the next and final section.
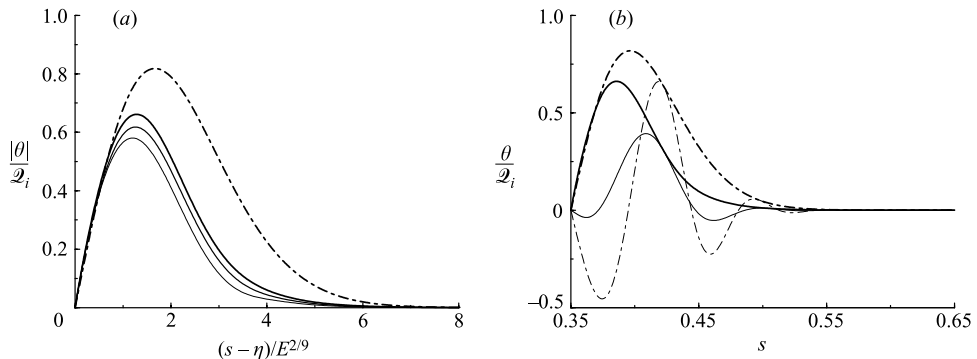
FIGURE 7. As in figures 6(*a*)(i) and (*b*)(i), except that the temperature, albeit scaled $\theta/\mathcal{Q}_i \equiv \eta^3\theta$, is plotted as in figure 3. The scaling is to aid comparison with figure 6.

6. Concluding remarks

The main conclusion is that our quantitative comparison between the asymptotic theory and the numerical solution of the full set of partial differential equations is generally excellent. To determine whether the asymptotic solutions at various orders are acceptable involves careful consideration of the data in the tables and the various graphical comparisons illustrated in the figures.

The scalings for the interior convective modes are much more straightforward than the tangent cylinder modes and simply involve expansions in powers of $E^{1/6}$. The interior modes consist of localized rolls width $O(E^{1/3})$, but elongated radially of length $O(E^{1/6})$. They are tilted to meridional planes at a finite angle $\tan^{-1}(-s_M k_M/m_c)$ ($\approx 34.2°$ for $P=1$) identified below (4.6). The term rolls is perhaps a misnomer as it reflects the nature of the instantaneous streamline pattern and not the fluid motion. Since our thermal Rossby waves are time dependent, the streamlines do not correspond to the particle paths.

The tangent cylinder convective modes are more awkward, involving expansions both in $E^{2/9}$ and $E^{1/3}$, as well as $E^{1/6}$ for the Ekman-layer corrections. Even ignoring the latter, this means that our expansion parameter is $E^{1/9}$. Their Airy function profile (3.20) leads to a structure which is quite distinct from the interior modes. So whereas interior modes are always tilted at a finite angle, the tangent cylinder modes are normal to the tangent cylinder and spiral to a finite angle as they enter the interior of the fluid. For the cases illustrated in figure 4, that tilt angle is evidently positive, just as in the case of the interior modes. Moreover, like the interior modes, their width is $O(E^{1/3})$ but unlike them their radial extent $O(E^{2/9})$ is shorter. Curiously, the number of intersections of the rolls with meridional planes determined by the Airy function structure (see e.g. (4.12)) is finite $O(1)$, whereas for interior modes (4.6) identifies the number to be $O(E^{-1/3})$.

Our claim, upon which we expand below, is that the $E^{2/9}$-convective layer is quasi-geostrophic and motion is blocked by the tangent cylinder from entering the interior ageostrophic regions. Evidently this must happen on the equatorial plane $z=0$, where fluid touches the inner sphere, and in that respect our equatorial plane plots in figures 3 and 6 are not particularly testing. For that reason, we have made similar plots in figure 8 of the full numerical solution on the spherical surface radius $r=(r_i+r_o)/2$ and compared them with those on the equatorial plane. The most striking feature is the almost total absence of disturbance on the spherical surface inside the tangent
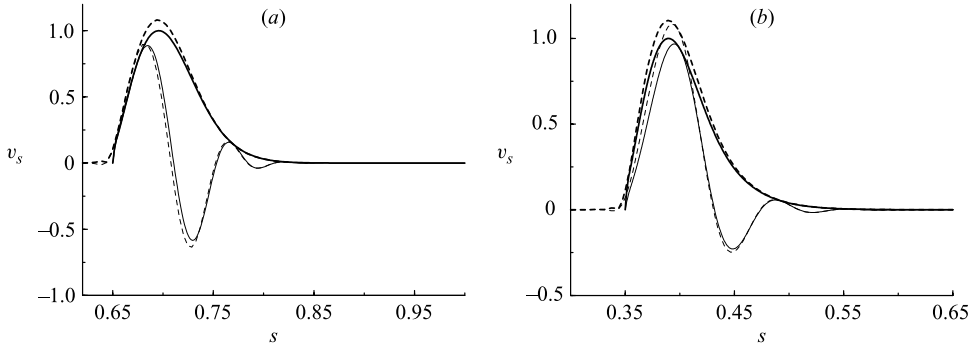
FIGURE 8. Plots of v_s, (*a*) in the case of internal heating with a large inner core (as in figure 3), and (*b*) in the case of differential heating (as in figure 6). The graphs show solutions of the full equations at $E = 10^{-7}$ for the case of stree-free boundaries. Results on the equator, $z = 0$ (given in figures 3 and 6) are identified here by the continuous lines, while the results on the sphere $(r_i + r_o)/2$ are identified by the dashed lines.

cylinder. In addition, the close coincidence of the convective solutions at $r = (r_i + r_o)/2$ and $z = 0$ outside the tangent cylinder confirms the columnar quasi-geostrophic nature of that solution.

Some comments are appropriate with regard to the tangent cylinder $E^{1/3}$-ageostrophic boundary layer. It is triggered because the boundary condition at $z = 0$ on the quasi-geostrophic eigenfunction $w(s, z)$ governed by (3.11) changes discontinuously from the symmetry condition $w(\eta, 0) = 0$ as $s \downarrow \eta$ to the zero normal velocity condition $\mathrm{d}w/\mathrm{d}z(\eta, 0) = 0$ as $s \uparrow \eta$. This is the feature noted by Busse & Cuong (1977) that leads to the jump of about a factor 4 in the value of the local critical Rayleigh number (noted in the Introduction) as the tangent cylinder is crossed inwards. Not only are conditions most unfavourable for convection within the tangent cylinder but the axial structure changes abruptly. This latter characteristic ensures that the s- and z-dependencies of the $E^{1/3}$-ageostrophic boundary layer are no longer separable in contrast to the quasi-geostrophic behaviour elsewhere. In other words, instead of solving an o.d.e. in z at each s for $w(s, z)$, a p.d.e. must be solved involving partial derivatives with respect to both s and z.

The nature of the $E^{1/3}$-ageostrophic boundary layer is determined by the properties of our $E^{2/9}$-convection layer solution (4.11) on the tangent cylinder $s = r_i$. There, correct to lowest order, our asymptotic solution (4.12) determines $\theta = 0$, $v_s = 0$ and $v_\phi = O(E^{1/9})$. The fact that only $v_\phi/E^{1/9}$ is non-zero is a most satisfactory state of affairs. It means that, correct to lowest order, the zero-amplitude solution inside the tangent cylinder has already been achieved just outside. Consequently, only a very weak $E^{1/3}$-ageostrophic boundary layer is required to make all the necessary adjustments. This idea is supported by our numerical results for $\theta/\mathcal{Q}$ and v_s portrayed in figures 3 and 6; remember that on the convection layer length scale the ageostrophic layer width is $x = O(E^{1/9})$, which for the numerical solutions portrayed, even with E as small as 10^{-7}, is larger than 0.1. Since, that is not a particularly small fractional horizontal extent, it could well account for features on the sensitive plots of $v_\phi/E^{1/9}$, whose asymptotic value on the tangent cylinder is non-zero, in contrast to those of $\theta/\mathcal{Q}$ and v_r which vanish. Arguably the positive x-displacement of the second and deeper minimum of the numerical results in the bottom row of graphs is $O(E^{1/9})$ is a manifestation of the ageostrophic layer. On the other hand, the abrupt divergence of

the numerical results for $v_\phi/E^{1/9}$ as $x \downarrow 0$ left of the first minimum must be associated with yet smaller sublayers, presumably of small axial z-extent, associated with the equator of the inner sphere.

Certainly, the above discussion lends support to the view that our terms neglected in the $E^{2/9}$-convection layer are $O(E^{1/9})$. Errors of that magnitude in our asymptotics are readily traced to the tangent cylinder boundary condition $\mathscr{W}(0) = O(E^{1/9})$ for the solution of (3.18). Unfortunately, the $O(E^{1/9})$ correction to the boundary condition can only be obtained by a solution of the boundary-layer equations governing the $E^{1/3}$-ageostrophic layer, which lies outside the scope of our present study.

Finally, we remark that the restriction of our analysis to the case of Prandtl number unity was simply to focus attention on the comparison of the asymptotic theory and the full numerical results. The interesting issue of the destabilizing $\mathscr{R}_{NS} - \mathscr{R}_{SF} < 0$ (stabilizing $\mathscr{R}_{NS} - \mathscr{R}_{SF} > 0$) role of the Ekman boundary layer for large (small) P is thus not addressed here but has been discussed elsewhere (Zhang & Jones 1993; Zhang 1995; in plane layer geometry, Zhang & Roberts 1998).

REFERENCES

ARDES, M., BUSSE, F. H. & WICHT, J. 1997 Thermal convection in rotating spherical shells. *Phys. Earth Planet. Inter.* **99**, 55–67.

BUSSE, F. H. 1970 Thermal instabilities in rapidly rotating systems. *J. Fluid Mech.* **44**, 441–460.

BUSSE, F. H. 1975 A model of the geodynamo. *Geophys. J. R. Astron. Soc.* **42**, 437–459.

BUSSE, F. H. 1994 Convection driven zonal flows and vortices in the major planets. *Chaos* **4**, 123–134.

BUSSE, F. H. 2002 Convective flows in rapidly rotating spheres and their dynamo action. *Phys. Fluids* **14**, 1301–1314.

BUSSE, F. H. & CARRIGAN, C. R. 1976 Laboratory simulation of thermal convection in rotating planets and stars. *Science* **191**, 81–83.

BUSSE, F. H. & CUONG, P. G. 1977 Convection in rapidly rotating spherical fluid shells. *Geophys. Astrophys. Fluid Dyn.* **8**, 17–44.

CARRIGAN, C. R. & BUSSE, F. H. 1983 An experimental and theoretical investigation of the onset of convection in rotating spherical shells. *J. Fluid Mech.* **126**, 287–305.

CHAMBERLAIN, J. A. & CARRIGAN, C. 1986 An experimental and theoretical investigation of convection in a rotating sphere subject to time varying thermal boundary conditions. *Geophys. Astrophys. Fluid Dyn.* **35**, 303–327.

CHANDRASEKHAR, S. 1961 *Hydrodynamic and Hydromagnetic Stability*. Clarendon.

CHRISTENSEN, U., AUBERT, J., CARDIN, P. ET AL. 2001 A numerical dynamo benchmark. *Phys. Earth Planet. Inter.* **128**, 25–34.

CORDERO, S. & BUSSE, F. H. 1992 Experiments on convection in rotating hemispherical shells: transition to a quasi-periodic state. *Geophys. Res. Lett.* **19**, 733–736.

DORMY, E. 1997 Modélisation numérique de la dynamo terrestre. IPGP PhD thesis.

DORMY, E., CARDIN, P. & JAULT, D. 1998 MHD flow in a slightly differentially rotating spherical shell, with conducting inner core, in a dipolar magnetic field. *Earth Planet. Sci. Lett.* **160**, 15–30.

GILMAN, P. A. 1975 Linear simulations of Boussinesq convection in a deep rotating spherical shell. *J. Atmos. Sci.* **32**, 1331–1352.

GREENSPAN, H. P. 1968 *The Theory of Rotating Fluids*. Cambridge University Press.

HART, J. E., GLATZMAIER, G. A. & TOOMRE, J. 1986 Space-laboratory and numerical simulations of thermal convection in a rotating hemispherical shell with radial gravity. *J. Fluid Mech.* **173**, 519–544.

HUERRE, P. & MONKEWITZ, P. A. 1990 Local and global instabilities in spatially developing flows. *Annu. Rev. Fluid Mech.* **14**, 473–537.

ISHIHARA, N. & KIDA, S. 2002 Dynamo mechanism in a rotating spherical shell: competition between magnetic field and convection vortices. *J. Fluid Mech.* **465**, 1–32.

JONES, C. A., MUSSA, A. I. & WORLAND, S. J. 2003 Magnetoconvection in a rapidly rotating sphere: the weak field case. *Proc. R. Soc. Lond.* A **459**, 773–797.

JONES, C. A., SOWARD, A. M. & MUSSA, A. I. 2000 The onset of thermal convection in a rapidly rotating sphere. *J. Fluid Mech.* **405**, 157–179 (referred to herein as JSM).

LAKSHMIVARAHAN, S. & DHALL, S. 1990 *Analysis and Design of Parallel Algorithms*. Mc Graw-Hill.

MEUNIER, N., PROCTOR, M. R. E., SOKOLOFF, D. D., SOWARD, A. M. & TOBIAS, S. M. 1997 Asymptotic properties of a nonlinear $\alpha\omega$-dynamo wave: period, amplitude and latitudinal dependence. *Geophys. Astrophys. Fluid Dyn.* **86**, 249–285.

ROBERTS, P. H. 1965 On the thermal instability of a highly rotating fluid sphere. *Astrophys. J.* **141**, 240–250.

ROBERTS, P. H. 1968 On the thermal instability of a rotating-fluid sphere containing heat sources. *Phil. Trans. R. Soc. Lond.* A **263**, 93–117.

SOWARD, A. M. 1977 On the finite amplitude thermal instability of a rapidly rotating fluid sphere. *Geophys. Astrophys. Fluid Dyn.* **9**, 19–74.

SOWARD, A. M. 2003 Thin aspect ratio $\alpha\Omega$-dynamos in galactic discs and spherical shells. In *Advances in Nonlinear Dynamo Theory* (ed. M. Núñez & A. Ferriz-Mas), vol. 9, pp. 224–268. Taylor & Francis.

YANO, J.-I. 1992 Asymptotic theory of thermal convection in rapidly rotating systems. *J. Fluid Mech.* **243**, 103–131.

ZHANG, K. 1991 Convection in a rapidly rotating spherical shell at infinite Prandtl number; steadily drifting rolls. *Phys. Earth Planet. Inter.* **68**, 156–169.

ZHANG, K. 1992 Spiralling columnar convection in rapidly rotating spherical fluid shells. *J. Fluid Mech.* **236**, 535–556.

ZHANG, K. 1995 On coupling between the Poincaré equation and the heat equation: non-slip boundary conditions. *J. Fluid Mech.* **284**, 239–256.

ZHANG, K.-K. & BUSSE, F. H. 1987 On the onset of convection in rotating spherical shells. *Geophys. Astrophys. Fluid Dyn.* **39**, 119–147.

ZHANG, K. & JONES, C. A. 1993 The influence of Ekman boundary layers on rotating convection in spherical fluid shells. *Geophys. Astrophys. Fluid Dyn.* **71**, 145–162.

ZHANG, K. & ROBERTS, P. H. 1997 Thermal inertial waves in a rotating fluid layer: exact and asymptotic solutions. *Phys. Fluid* **9**, 1980–1987.

ZHANG, K. & ROBERTS, P. H. 1998 A note on stabilising and destabilising effects of Ekman boundary layers. *Geophys. Astrophys. Fluid Dyn.* **88**, 215–223.